Article

Biomolecular Interaction of Carnosine and Anti-TB Drug: Preparation of Functional Biopeptide-Based Nanocomposites and Characterization through In Vitro and In Silico Investigations

Usharani Nagarajan, Aniket Naha, Gayathri Ashok, Angayarkanni Balasubramanian, Sudha Ramaiah, Swarna V Kanth, Azger Dusthackeer, Anand Anbarasu,* and Saravanan Natarajan*

Cite This: *ACS Omega* 2025, 10, 567–587

Read Online

ACCESS | Metrics & More | Article Recommendations | Supporting Information

ABSTRACT: Host-directed therapies (HDTs) resolve excessive inflammation during tuberculosis (TB) disease, which leads to irreversible lung tissue damage. The peptide-based nanostructures possess intrinsic anti-inflammatory and antioxidant properties among HDTs. Native carnosine, a natural dipeptide with superior self-organization and functionalities, was chosen for nanoformulation. In the present work, multiscale self-assembly approaches of carnosine were developed using a solvent-mediated process (hexafluoro-2-propanol) and further linked with first-line anti-TB drugs. The organofluorine compound in a solvent is attributed to the self-assembling process with heteroatom acceptors in carnosine. In the carnosine-anti-TB drug nanocomposite, the functional moieties represent the involvement of hydrogen bonding and the electrostatic force of attraction. The minimum inhibitory concentration of carnosine-anti-TB drug composites represents an antimycobacterial effect on par with standard drugs. The silicon findings complemented the in vitro results through quantum chemical simulations, elucidating the respective binding pockets between putative *Mtb* drug targets and carnosine-anti-TB composites. These findings confirmed that the carnosine and anti-TB drug nanocomposites prepared through a solvent-mediated process act as a rational design for functional nanodelivery systems for sustainable TB therapeutics.
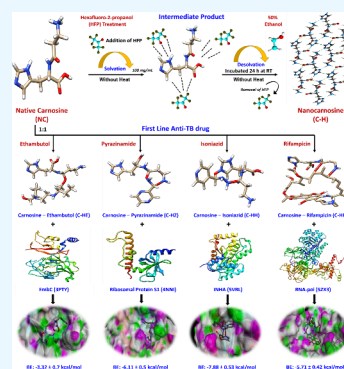
1. INTRODUCTION

Tuberculosis (TB) is the second leading infectious disease from a single infectious agent, after COVID-19.[1] According to WHO report 2022, the TB death rate fell until 2019, followed by an increase in 2020 and 2021, as evidenced in four of the six WHO regions.[2] This creates a pressing situation to boost the recovery rate of TB patients owing to its prolonged duration of therapy, high pill burden, poor patient compliance, and stringent management regimens in the treatment of TB.[3] In TB chemotherapy, the introduction of nanotechnology has gained a broader scope in diagnosis, treatment, and delivery mechanisms. Compared to parenteral or oral deliveries, nanodelivery of drugs through pulmonary mode reaches directly to alveolar macrophage, which is the primary site for TB infection and localization of *Mycobacterium tuberculosis* (*Mtb*).[4] In the recent past, the choice of peptides has been repurposed for the delivery of conventional drugs for treatment regimens. The molecular self-organization of these peptides is significant in generating functionalized materials with biomimetic properties.[4] Still, challenges exist in the development process, such as the production cost, the availability of raw material, and enhanced biodegradability in the case of peptide research. Considering this, carnosine, a natural dipeptide with intrinsic anti-inflammatory and antioxidant properties, was chosen for the study. As a naturally occurring endogenous dipeptide, carnosine has proven to perform well-demonstrated

multiaxial functions such as balancing the reactive oxygen species, pro-inflammatory regulation, and modulating immunometabolic behavior of cells. Moreover, researchers have extended protective activities in various cell types such as heterogeneous cells, microglial, endothelial cells, stem cells, etc. In particular, they were found to be more effective in the case of macrophages and microglia.[5]

Carnosine possesses distinct functional properties such as neutralizing harmful free radicals in the host (antioxidant balance), reducing inflammation in various tissues (pro-resolving pathways), capable of protecting the brain cells by evading the brain blood barrier (neuroprotective benefits), reversing the formation of antiglycation activity, and also ameliorating the endurance of muscle properties and decreasing the fatigue during stress conditions.[6] The combinatorial effect of carnosine in the supplementation and therapeutic use makes it more versatile and benign than other therapeutic peptides. These biofunctions of carnosine highlight

the need for choosing this peptide for the study, and its benefits are not obvious in the case of other peptides.

In the current work, a tailor-made process was carried out to form functional nanostructures from native dipeptide oligomers (carnosine) along with anti-TB drugs using an organic solvent, hexafluoroisopropanol (HFP), for potential application in pulmonary tuberculosis. HFP may induce self-assembled structures that provide different morphologies for the carnosine anti-TB drug nanocomposites during solvent evaporation. The backbone structure of the carnosine nanopeptide is preserved despite the induction of a secondary structure (α-helix).[7] HFP exhibits a high hydrogen bonding donor ability, low nucleophilicity, and high ionizing capacity to solvate water, and its effect on organic transformations activates the oxidation reactions.[8]

Using a multiscale self-assembly approach, we have developed and characterized the carnosine dipeptide and anti-TB drug [rifampicin (RIF), isoniazid (INH), pyrazinamide (PYZ), and ethambutol (EMB)] nanocomposites for the potential therapeutic application in pulmonary tuberculosis. The significance of solvent treatment mediates strong hydrogen bonds between the functional moieties of carnosine and the heteroatoms of anti-TB drugs.[9] This is the first report on the orientation of carnosine dipeptides with anti-TB drugs to form carnosine anti-TB drug nanocomposites using a solvent-mediated process projected for the treatment application in pulmonary TB. Moreover, the solvent-mediated self-association of carnosine with anti-TB drugs represents a novel architecture in the nanoscale.[10]

The interactions of carnosine dipeptide-anti-TB drugs are likely to promote self-assembly inducing structure stability and thereby play a crucial role in shaping the energy landscape and phase behavior of dipeptides. The *in silico* analysis was intended as a unique approach to evaluate the anti-TB efficacy of the classical drugs in conjugation with carnosine, a potent delivery vehicle for anti-TB drugs. Therefore, the carnosine-anti-TB drug conjugates were modeled based on the in vitro experimental results and were further optimized to generate stable structures as a first of its kind. The conjugate ligands (anti-TB drug molecules) were thereafter subjected to molecular docking analysis to predict the intermolecular interactions with their respective TB drug targets. The drug molecule ligands with high binding affinity toward *Mtb* target receptors were further scrutinized through quantum chemical simulations to elucidate the reactivity parameters between them. The resulting binding moieties may reflect better therapeutic entities and associated pharmacokinetics parameters. Molecular dynamics simulations (MDSs) were performed to establish the stable complexes formed between protein targets and ligand drugs.[11−21] Taken together, this work paves the way for new avenues in the preparation of nanostructures through peptide self-assembly and demonstrates the diversity of the peptide structure with no chemical modifications. The intermolecular forces driving the self-assembly process of carnosine and anti-TB drugs subjectively represent an important route to the rational design of functional nanomaterials for a new mode of administration.

2. MATERIALS AND METHODS

2.1. Materials. Chemicals were purchased from Sigma-Aldrich Chemicals, Bangalore, India. The instrumental analysis were carried out at the Council of Scientific and Industrial

Research-Central Leather Research Institute (CSIR-CLRI), CATERS, Chennai, India.

2.2. Solvent-Mediated Extraction Process. The carnosine nanostructures (C−H) from native carnosine (NC) were prepared using a modified method of Arul et al.[22] The carnosine dipeptide stock solution was dissolved in HFP to the appropriate concentration (100 mg/mL). Further, the peptide stock solution was diluted (5 mg/mL) in ethanol (50%) and incubated overnight, facilitating the self-assembling process.

2.3. Preparation of Hybrid Carnosine-Anti-TB Drug Nanocomposite. Carnosine (0.4 M) interacted with anti-TB drugs (RIF, INH, PYZ, and EMB) (1:1 ratio) to obtain nanocomposites such as carnosine−RIF (C-HR), carnosine−INH (C-HH), carnosine−PYZ (C-HZ), and carnosine−EMB (C-HE) and freeze-dried (stored at −20 °C).[23]

2.4. Characterization of Solvent-Mediated Carnosine Nanoclusters and Carnosine-Anti-TB Drug Composites. *2.4.1. Secondary Structural Arrangements Using Circular Dichroism.* The influence of the solvent-mediated process over the conformational changes in the nanostructures was studied using circular dichroism (CD, J-815 spectropolarimeter (JASCO), Gross-Umstadt, Germany). The CD spectra were recorded from 190 to 280 nm at the rate of 50 nm/min, and the data were normally plotted as mean-residue-weight ellipticity (° cm^{2}dmol^{-1}) versus wavelength.[24]

2.4.2. Functional Group Analysis Using (FTIR): Side Chain Modifications. FTIR measurements for NC and C−H were performed by a PerkinElmer−Spectrum Two FTIR spectrometer measuring 400−4000 cm^{-1} with a maximum of 100 scans.[25]

2.4.3. Structural Phase Identification Using (XRD): Nature of the Product. The powder X-ray diffractograms of NC and C−H were obtained using a Mini Flex-II desktop X-ray 162 diffractometer (Rigaku, Japan) with the source of Cu Kα radiation (λ = 1.54 Å) at 30 kV and 15 mA in the range of 5−80° (2θ) at the rate of 4°/min. The relative crystallinity of dipeptide samples was quantitatively estimated in the region 2θ = 5−50° using Origin Pro 8.0 (Origin Lab, USA).[26]

2.4.4. Specific Surface Area and Porosity Distribution Using Brunauer−Emmett−Teller Analysis. The measurements of N$_2$ absorption−desorption isotherms of the solvent-mediated carnosine (C−H) at (78 K) and gas saturation vapor tension was obtained using the ASAP 2020 V4.03 (V4.03H) static volumetric absorption analyzer (Micromeritics Corp., NY, USA). Nanopreparation (0.1 g) was set to degas (2 h) at 22 °C with the analysis bath temperature 196.2 °C at an equilibration interval of 10 s in flowing nitrogen. This degassing removes contaminants such as water vapor and adsorbed gases from the samples. The static physisorption isotherms were obtained with N$_2$ and recorded as adsorption, or desorption from the material as a function of pressure (P/P_o).[27] As adsorption or desorption occurs, the pressure in the sample cell changes until an equilibrium is reached. The specific surface area of the solvent-mediated dipeptide was calculated using the Barrett−Joyner−Halenda (BJH) academic model from the Brunauer−Emmett−Teller (BET) adsorption equation.[10,28]

2.4.5. In Vitro Cytotoxicity Evaluation. 2.4.5.1. Cell Culture. Dulbecco's modified Eagle medium [10% fetal bovine serum + glutamine (2 mM) + penicillin (100 U/mL)/streptomycin (100 mg/mL) + fungizone (0.25 mg/mL)] was used to culture 3T3 cell lines and incubated at 37 °C (5%

CO$_2$). The confluent flask was trypsinized, and the obtained cells (3.5 × 10^3) were added to 50 mL of culture medium.[29]

2.4.5.2. MTT Assay. The percentage of cell viability was analyzed using MTT colorimetric assay. Briefly, the normal cell viability was inferred from the reduction of MTT, [3-(4,5-dimethylthiazol-2-yl)-2,5-diphenyl-2H-tetrazolium bromide] to purple formazan crystals. NC & C−H (100, 50, 25, 12.5, 6.25, 3.125, 1.565, 0.78125 μg/mL) were incubated with 100 mL of MTT (1 mg/mL in PBS) for 4 h. Dimethyl sulfoxide (100 mL) was added to solubilize formazan crystals and measured using an ELISA reader (550 nm). The percentage of cell viability was expressed from the mean values calculated against control samples.[30]

2.4.6. Size Measurements Using DLS. Particle size measurements of NC, C−H, and anti-TB drug composites such as C-HR, C-HH, C-HZ, and C-HE were performed at 25 °C using a dynamic light scattering (DLS) analyzer (Malvern Nano-Zetasizer ZS, Malvern, UK).[31]

2.4.7. Thermal Stability Using Differential Scanning Calorimetry. A high-sensitivity thermogravimetric analyzer (TA Instruments, Waters Austria Model No.Q200) was used in a nitrogen atmosphere, and the spectra were recorded at a scan rate of 10 °C/min up to 300 °C (gradual increase). Samples of NC, C−H, and carnosine−anti-TB drug nanocomposites (C-HR, C-HH, C-HZ, and C-HE) were weighed (~5 mg) in an aluminum pan which is precalibrated with indium with the supply of nitrogen gas at a rate of 45 mL/min.[32] Analysis was carried out using Mettler STARe software, version 8.10.

2.4.8. Contact Angle Measurements. A drop shape analyzer was used for contact angle (θ) measurements of NC, C−H, and carnosine−anti-TB drug nanocomposites (Kruss Drop Shape Analysis, Hamburg, Germany). The peptide-drug formulations (20 μL) were filled in a Hamilton syringe to dispense a drop on a glass slide at ambient conditions. The spreading coefficient measurements were calculated using Kruss software and presented as mean values from triplicates.[33]

2.4.9. Morphological Analysis. The morphological features of the NC, C−H, and carnosine−anti-TB drug nanocomposites were investigated using scanning electron microscopy (SEM) (VEGA3 TESCAN, Japan). The thin layer of peptide-drug samples was spread on an aluminum stud and gold-coated to prevent electron beam charging.[10]

2.4.10. Antimycobacterial Activity of Carnosine Nanoclusters and Carnosine-Anti-TB Drug Nanocomposites. *2.4.10.1. Test Organisms.* *Mtb* H37Rv (H37Rv) was used for performing the antimycobacterial activity of carnosine nanoclusters-anti-TB drug composites. The strains were subcultured in Lowenstein Jensen (LJ) media and collected for validation during the growth log phase. Spot inoculation into brain-heart infusion (BHI) agar plates was used to ensure there was no contamination. To ensure safety and containment, all tests were conducted at the BSL3 laboratory, which is located in the Bacteriology Department at the ICMR-NIRT, Chennai-31.

2.4.10.2. Determination of MIC by Broth Dilution Method. A suspension of H37Rv was taken in a biju bottle containing glass beads in Middlebrook 7H9 medium enhanced with 10% OADC (7H9). To get rid of the clumps, the suspension was vortexed vigorously and allowed to stand for 30 s to settle the aerosol. One McFarland (1 MF) matching culture suspension was diluted to a 1:20 ratio using 7H9. The minimum inhibitory

concentration (MIC) of standard drugs (RIF, INH, PYZ, and EMB) and carnosine-drug composites (C-HR, C-HH, C-HZ, and C-HE) against H37Rv was determined at different concentrations. A hundred microliters (100 μL) of 7H9 was dispensed in a flat bottom 96-well plate along with 100 μL of drug composites in different concentrations and serially (2-fold dilution) diluted. Finally, 100 μL of culture suspension from 1:20 dilution was added in all wells and incubated for 14 days at 37 °C with 5% CO$_2$. After 5 days of incubation, the plates were observed under the microscope for growth based on the serpentine chord formation of *Mtb* culture growth. All tests were performed in duplicate on a microtiter plate and analyzed for the nanocomposite MIC concentration which could inhibit the growth of *Mtb* completely or 90%.[34]

2.5. In Silico Approach in Determining the Antimycobacterial Effect of Carnosine-Drug Nanocomposites. *2.5.1. Ligand Structure Retrieval and Coarse Optimization of Drug Leads.* The 3D structures of the classical anti-TB drugs were retrieved from the PubChem Database which includes EMB (PubChem CID: 14052), PYZ (PubChem CID: 1046), INH (PubChem CID: 3767), and RIF (PubChem CID: 135398735). The structures with 2D coordinates were converted to 3D-coordinated structures from the Open Babel Chemical File Format Converter server using atomic valences and satisfied upon adding polar hydrogen atoms.[35] The ligand structures were subjected to coarse optimization to attain optimal spatial orientation with minimal torsions, stable bond lengths, bond angles, and dihedrals under universal force-field mechanics restraints using Avogadro v1.2.0 software.[36] However, the optimized structure of carnosine was procured from our previous work which was optimized with the B3LYP functional and the 6-311G + + (d,p) basis set.[10]

2.5.2. Ligand-Ligand Docking and Formation of Ligand Conjugates. Carnosine-anti-TB complexes were generated upon performing ligand−ligand docking through the Seam-Dock server which provides an interactive small compound molecular docking.[37] The dipeptide carnosine molecule was considered as the receptor which was centered inside the docking box, while protonation was attained using the Propka method which is computed with the *pdb*2pqr python library module using the *prepare_receptor4.py* scripts. The classical anti-TB drugs were calibrated upon subjecting the molecules to the rdkit function *MMFFOptimize Molecule* module under Merck molecular force-field mechanics (MMFF94) under a maximum iteration of 200. Finally, the ligands were processed with the *prepare_ligand4.py* scripts from AutoDock Tools, and subsequently docking and scoring algorithms were executed through computing autogrid (*prepare_gpf4.py*) and computing the grid (*prepare_dpf4.py*) from MGL Tools suite, respectively. The ligand−ligand complex was therefore retrieved and subjected to further molecular docking, quantum chemical simulations, and MDS analyses.

2.5.3. Optimization of Drug Target, Domain, and Druggability Predictions. The putative drug targets from *Mtb* were considered from our previous research work which serves as the classical drug targets for EMB (arabionosyl transferase C-terminal domain; PDB ID: 3PTY), for PYZ (ribosomal protein S1; PDB ID: 4NNI), for INH (enoyl ACP reductase INHA; PDB ID: 5VRL), and for RIF (RNA polymerase C-chain; PDB ID: 5ZX3).[16,18] The missing residues in these drug targets were further cured upon performing a template-based modeling approach using the SWISS-MODEL server considering these PDB proteins as

templates.[38] Thereafter, the modeled proteins were energy refined to enhance the Ramachandran parameters using the Galaxy Refine server which optimized structural patterns upon packing and repacking the side chains.[39] Energy minimization was performed *in-vacuum by* carrying out 2000 steps each for steepest-descents and conjugate-gradients algorithms with GROMOS96 43B1 force-field mechanics using standalone Swiss-PDB Viewer v4.1.0 software.[40] The global energetics were assessed from the ProSA-web server concerning the protein backbone ($C\alpha$-atoms) through energy plots that revealed local model quality by considering each amino acid residue with energy functions, where the positive values signify erroneous conformations and negative values indicate proper folding with minimal errors.[41] Tertiary structural validations were carried out upon assessing Ramachandran plot parameters, side chain conformations, planar peptide bonds, polarity of residues, and several atom−atom outliers. The functional and catalytic domains of the protein targets were studied and validated from the InterPro and Pfam servers.[42,43] Finally, the surface topology of the proteins was scanned to examine the potential drug-binding grooves that can serve as the active-site pockets for the interacting ligands through the CASTp server.[44] The druggability of these pockets to decipher their drug-binding probability was assessed from the PockDrug server.[45]

2.5.4. Molecular Docking and Intermolecular Interaction Analysis. The optimized drug targets (receptors/macromolecule) and ligands (classical anti-TB drugs and carnosine-anti-TB drug conjugates) were docked using AutoDock 4.2 and its embedded tools that use semiempirical free energy scoring function to predict the binding energies of docked poses with high reproducibility.[46] The receptor molecule (with polar H atoms, merge nonpolar H atoms, and Kollman charges) was prepared for docking. The ligand torsions were also fixed upon merging nonpolar H atoms and the addition of requisite Gasteiger charges. Thereafter, the receptor was centered inside the affinity grid box of dimensions 126 Å × 126 Å × 126 Å and uniform grid-point spacing of 0.375 Å. Finally, *autogrid4* and *autodock4* programs were executed that respectively scanned and generated the docked protein−ligand complex. Lamarckian and genetic algorithms were opted for selecting complexes with the least binding energy. Molecular docking was performed in triplicates, and the binding energy is expressed as mean ± SD.[11,12,15] Visualization of the 2D docked pose was done using the standalone Discovery Studio Visualizer v20.1.0.19295[47] highlighting various canonical and noncanonical intermolecular interactions established between the drug with its respective targets, while the 3D conformer of the protein−ligand docked complexes was visualized in standalone UCSF-Chimera v1.9.[48]

2.5.5. Quantum Chemical Simulations Using Density Functional Theory Calculations. Based on the binding energies and intermolecular interaction patterns, the drug conjugates which possessed better binding affinity as compared to the classical drug alone were further optimized through quantum chemical simulations to decipher their chemical reactivity and structural stability parameters. Ligand optimization was carried out using a standalone Gaussian-09 computational chemistry software package and visualized in GaussView v6.0.16 software.[49,50] The simulations were carried out in a Dell Precision Tower 3660 Workstation with 12th Generation Intel Core i9−12900 with 2.40 GHz processor and 32GB RAM layout.

The molecular geometry optimization of both the leads was performed using hybrid density functional Becke's three-parameter exchange-correlation (B3) conjugated with the Lee−Yang−Parr (LYP) and 6-311G + + (d,p) basis level for estimating its minimal energy configurations.[51] The current basis set was selected as the polarization of atomic orbitals was achieved where the p-type functional was added onto all hydrogen atoms. Diffuse functional (d-type) was used since all of the studied molecules possessed nitrogen and oxygen that possessed lone pairs of electrons.[52] Further, the intrinsic properties and chemical reactivity of the drug molecules were examined through natural bond orbital (NBO), frontier molecular orbitals (FMOs), molecular electrostatic potential (MEP), and global descriptors.

The NBO analysis substantiates the charge delocalization from bonding (donor) to antibonding (acceptor) orbitals. The bonding−antibonding interactions contributed by the 'electronegative donor atomic orbitals (i)' to 'electron-deficient acceptor atomic acceptor orbitals (j)' impart molecular stability of the lead. The stability is determined based on the Fock matrix derived from the second-order perturbation theory and is expressed in terms of stabilizing energies ($E^{(2)}$). Global descriptors calculated under the same B3LYP/6-311G + + (d,p) basis set described the overall properties and characteristics of the molecule, which could be analyzed from the energy profiles and energy gap (ΔE) displayed by FMOs. The highest occupied molecular orbital (HOMO) and the lowest unoccupied molecular orbital (LUMO) explain the overall electron affinity (A) and ionization potential (I) of the molecule. Other global descriptors explained through electronegativity (χ), chemical potential (ρ), chemical hardness (η), softness (δ), global electrophilicity index (ω), and electron-withdrawing ($\omega-$) and donating ($\omega+$) power are calculated based on Koopman's Theorem.

2.5.6. MDS. The stability of the protein−ligand complexes was further adjudged upon studying their dynamicity over a time frame of 50,000 ps using the GROMACS 2020.2 suite. The topology of the drug targets was built with CHARMM36-Feb2021 force-field mechanics and a simple-point charge water model (TIP3P), while ligand topology was built using the CGenFF server. Further, the complex was centered inside a dodecahedron box of a uniform edge distance of 1.0 nm following solvation with a simple-point charge water model. System neutralization was achieved with requisite counterions (Na^+/Cl^-). Steepest-descents algorithm (50,000 steps) and convergence-tolerance force (1000 kJ/mol nm^{-1}) were considered for energy minimization of the system. Thereafter, two cycles of equilibrations opted with constant volume (NVT) ensemble for 100 ps using leapfrog integrator for attaining the desired temperature (300 K). Second, a constant pressure (NPT) ensemble for 100 ps using the Parrinello−Rahman barostat was applied to attain the desired pressure (1 bar) upon applying motion equations to the box vectors. Long-range electrostatic interactions were treated using the particle-mesh Ewald algorithm with a cubic interpolation on the order of 4.0 and Fourier spacing of 0.16 nm. Finally, the system was subjected to MD production for a 50,000 ps time scale with an integration time scale of 2 fs and sampling of simulated trajectories was carried out every 10 ps.[12,16,53−55]

2.5.7. MDS Trajectory Analysis. MDS was interpreted through several trajectory analyses, which enabled interpretation of the stability through the deviations and fluctuations of the protein backbone ($C\alpha$ atoms). The trajectories were

analyzed through several programs and visualized using Grace software. In the current study, the stability of the complexes was interpreted from RMSD (*gmxrms*), while the residue-level fluctuations were deciphered through the RMSF (*gmxrmsf*) analysis. The compactness of the complex was analyzed from the radius of gyration (Rg; *gmx gyrate*) analysis, while the energetic (*gmx energy*) of the system indicating optimal equilibration was checked from the potential energy curve. The intermolecular interaction pattern highlighting the H bonds from molecular docking was further validated from MDS using the *gmxhbond* program, and the concerned interaction energy was also evaluated. The formation of uniform solvation is determined from the solvent-accessible surface area, and the free energy of solvation (ΔG_{solv}) was determined using the *gmxsasa* program. Last, the functional domains of the proteins and the inhibitor drug molecules are found concurrent with atomic level fluctuations to understand structure–function relationships.[12,16,53]

3. RESULTS AND DISCUSSION

In the present study, we have developed nanocomposites using carnosine and anti-TB drug conjugates and evaluated their appropriateness for host-directed therapy through *in vitro* and *in silico* approaches including antimycobacterial properties. The first line of anti-TB drugs was treated with carnosine through a solvent-mediated process. Each drug (RIF, INH, PYZ, and EMB) was allowed to interact with carnosine in a 1:1 ratio and evaluated for its interaction efficiency with the carnosine molecule. As per the method described in Section 2.1, through the solvent-mediated process, the composites of NC and drugs in the presence of HFP were treated and processed to obtain lyophilized drug composites such as C-HR, C-HH, C-HZ, and C-HE, which were further characterized biophysically and biochemically.

In the literature, *in vivo* models have been used to confirm the extended bioavailability by the usage of selective inhibitor systems (carnosinases). The degradation ability of the peptide has been studied extensively by varying the functionalization of the dipeptides. The preclinical experiments relating to the intranasal administration of carnosine are expected to bypass the first pass metabolism, hence the bioavailability is more and the degradation or the elimination protocol remains seamless.[56] The optimum pH for hydrolysis of carnosine was shown to be pH 7.5 and 8.5, and a complete degradation with a maximum of pH 9.5 was reported by Jackson et al. The interaction system of carnosine with dipeptides was optimized close to the isoelectric point at pH 6.5–7. We see a more stable structure with intact hydrogen and the electrostatic force of attraction. This has been confirmed through functional group annotation, potential surface charge analysis, thermal stability, and morphological variations. Moreover, the prepared nanocomposites were stored in subzero level, and continuous alterations in structural stability were confirmed through morphology analysis.[57]

3.1. Characterization of Solvent-Mediated Carnosine Nanoclusters and Carnosine-Anti-TB Composites.
3.1.1. Secondary Structural Conformation of Carnosine Nanostructures (C–H). Self-assembled structures of NC and C–H obtained from the CD spectrum align into ordered structures. The CD spectrum for 1% NC is characterized by a single positive peak at ~217 nm and a negative peak around ~197 nm (Figure 1a). The intramolecular stacking interactions lead to nπ* transition (219 nm) of the imidazole ring, evident
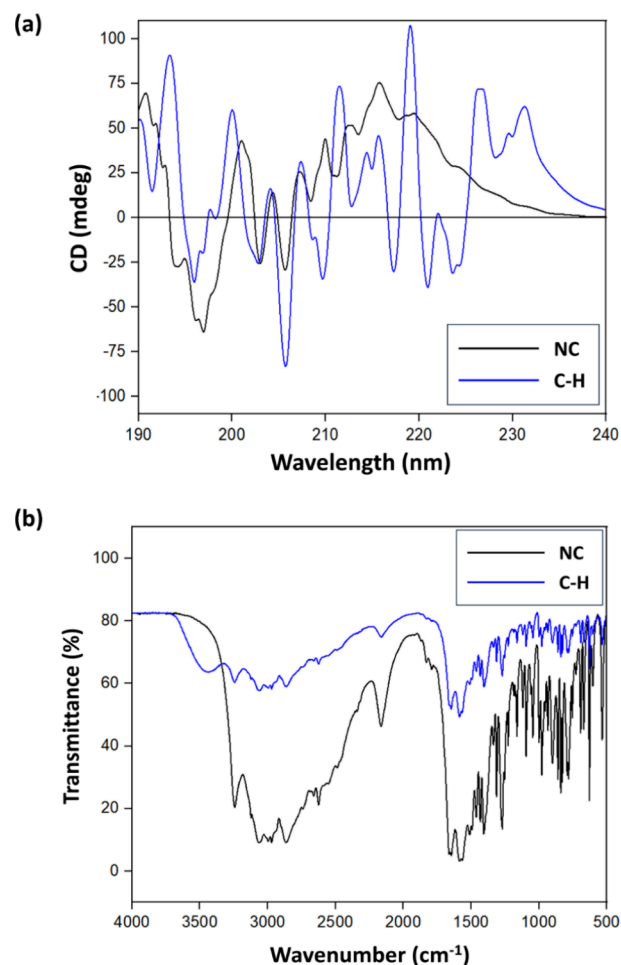

Figure 1. Structural changes in NC and solvent-mediated carnosine nanostructures C–H. (a) CD spectra and (b) FTIR spectra.

for short peptides containing aromatic residues. However, the C–H spectrum shows representation of the random coil due to disruption in hydrogen residues characterized by maximum positive peaks at ~210–219 nm. Consequently, negative peaks around ~196–224 nm represent alterations in the conformations due to binding interactions and positioning of the imidazole moiety. The β-sheet conformations may be diverse in multiple peak positions because they occur either in parallel or antiparallel with twisted directions (Figure 1a).

3.1.2. Vibrational Spectroscopy. The vibrational FTIR spectrum (Figure 1b) of NC exerted terminal amine in the N13 position at 3249 cm^{-1}, COO-stretchings around 2800–2207 cm^{-1}, C=O stretchings in the region 1860–1353 cm^{-1}, and subsequent amine bending in 1332–1312 cm^{-1} and CH–NH stretchings around (1215 and 1063 cm^{-1}, Nπ, C2, and Nτ), respectively (Figure 1b). In the case of C–H, the structural conformation shift in the region around 3418–3609 cm^{-1} represents the OH bonding stretchings, correspondingly representing the solvent mediation leading to broadening of the terminal amine position. In addition, peaks corresponding to in-plane bending C=O (1772 cm^{-1}) and the amine-methylene group (1210 cm^{-1}) can also be assigned in this region of the NC spectrum, with slight variation in the stretching position. Nevertheless, C–H shows a similar backbone spectrum of NC with a slight difference in the overall intensity. The stretching position with excess OH groups appears due to the solvent addition.

3.1.3. Diffraction Pattern Analysis. The secondary structural orientations in the carnosine nanostructures developed due to the solvent extraction process were explained using the XRD spectrum of NC and C−H. The pattern of NC exerted maximum peaks around 10.9, 19.98, 20.35, 22.35, 24.59, and 27.42°. The strong $\pi-\pi$ interactions due to stacking resulted in the *d* spacing of 1.811 3.70, 3.90, 3.96, 3.48, and 2.75 Å. Whereas the pattern of the C−H peak formed around 11.17, 19.92, 21.32, 22.55, and 24.38° with the *d* spacing of 2.89, 4.14, 3.55, and 1.29 Å (Figure 2). Here, the analysis
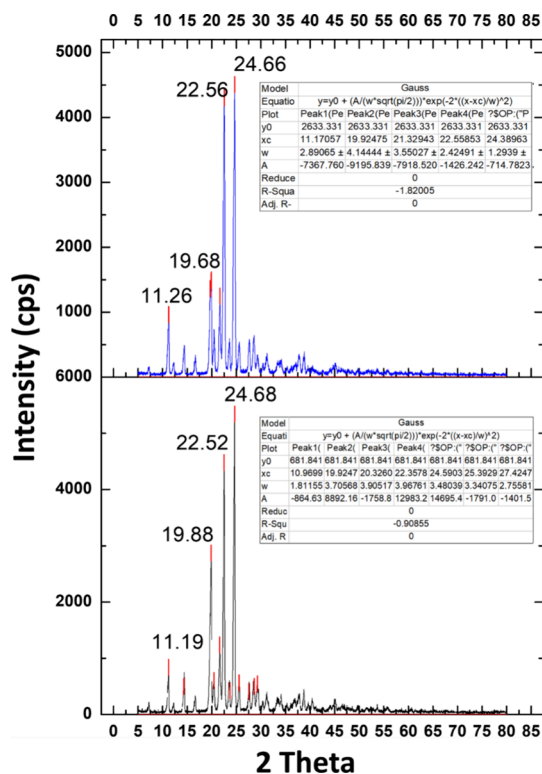

Figure 2. XRD pattern of NC and C-HFP-mediated carnosine.

indicated that the XRD peak position and width are the same in NC and C−H but slightly vary with the intensity of the peak. The high peak intensity in NC represents higher crystallinity and larger crystal size, while the low peak intensity of C−H explains the smaller crystal size, which was confirmed by the FTIR and CD data.

3.1.4. Surface Area Measurements. The surface parameter of C−H was studied using nitrogen adsorption/desorption isotherms at 77 K using BET analysis (Table 1). The obtained

Table 1. Surface Area Measurements of C−H

sl. no.	factor		unit
1.	Surface Area		3.29 ± 0.03 **m^2/g**
2.	Average Diameter		**35.9 nm**
3.	Molecular Cross-Sectional Area		0.1620 nm^2
4.	BJH Cumulative surface area	Adsorption	1.883 m^2/g
		Desorption	1.3740 m^2/g
5.	BJH Cumulative volume of pores	Adsorption	0.028 mm^3/g
		Desorption	0.0033 mm^3/g
6.	BJH Adsorption average pore diameter	Adsorption	60.3411 nm
		Desorption	9.6 nm

surface area of C−H is ~3.29 m^2 g^{-1} based on the BET model. The average diameter of C−H measured is about 35.9 nm. Moreover, the adsorption and desorption rates of C−H were attributed to mesoporosity suggesting the concrete spacing in the interaggregate spacing of C−H.[58]

3.1.5. Cytotoxicity Evaluation. The cytotoxic evaluation of NC and C−H on the human fibroblast 3T3 cell line was done at decreasing concentrations that range from 100 to 0.81 μg/mL (Figure 3). The cell viability for the NC concentrations 100 and 0.81 μg/mL were 90 and 78%, respectively. In the case of C−H, cell viability was 85% with 100 μg/mL and 70% with 0.81 μg/mL. This indicates that carnosine dipeptide favors the cell viability even after solvent treatment and makes it way suitable for its plausible application for pulmonary delivery in the host.

3.1.6. Size Determination of Carnosine Nanoclusters and Carnosine-Anti-TB Clusters. The data presented in Table 2 show that the solvent-mediated carnosine nanoclusters (NC and C−H) can self-assemble into narrow structures as evident from the poly dispersity index (PDI) values. These dipeptides such as NC possess high electron density measuring a significantly larger average size of about ~952 nm compared with C−H (~354 nm). This can be attributed to the fact that NC with free negatively charged head groups possesses a relatively larger hydrodynamic radius (due to electrostatic repulsion). Moreover, the conductivity of the samples is also increased with the solvent-mediated process.

The surface-to-volume ratio of nanocomposites is expected to get absorbed into the alveoli without getting adsorbed along the air passage in the lungs. Table 2 shows that the carnosine-anti-TB nanocomposites were prepared using solvent-mediated process measuring about ≤2 μm in solution. The formation of aggregates explains the drug interaction with the functional moiety of carnosine. The anti-TB drugs with available free functional groups tend to interact with carnosine's free −C≡O− and −NH$_2$− end by either hydrogen bonding or noncovalent interactions. In addition, zeta potential measurements suggest that the electrostatic force of attractions also plays a major role in holding the molecules together. Moreover, the polydispersity of carnosine-anti-TB drug nanocomposites measured about ≤1. This confirms that the drug complexes were mostly homogeneous in solution. The hydrodynamic diameter of the composites suggests the aggregated motion of particles in solution vs scattering methods.

3.1.7. Thermal Stability Measurements. Thermal transitions in the crystallinity of NC and C−H were investigated using scanning calorimetric thermograms. An endothermic peak at 270 °C was seen as indicative of carnosine melting. C−H exhibited a slightly lesser melting temperature at 268.4 °C (Table 2). The changes in the structural moiety within the peptide molecule are represented as a broad endothermic peak with enthalpy around 617.2 J/g (NC) and 258.6 J/g (C−H). These endothermic peaks represent a minute alteration in the nanosuspensions based on the structure, stability, and affinity of peptide molecules due to solvent-mediated processes.

3.1.8. Wetting Parameter of Carnosine Nanoclusters and Carnosine-Anti-TB Drug Nanocomposites. The suspension of NC and C−H was determined for its solid surface wettability through contact angle measurements. The surface parameter such as roughness and topology of the substrate was determined through angle of deviation from the wetting of NC and C−H. The average contact angle value of NC and C−
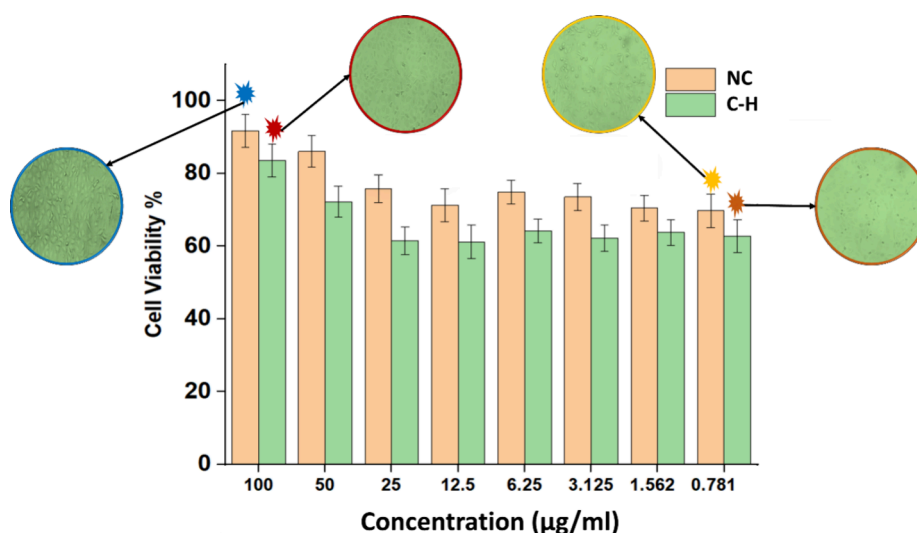
Figure 3. Percentage of the cell viability of NC and C−H.

Table 2. Size Determination and PDI of the Carnosine-Drug Composite Using Solvent-Processed Carnosine and Carnosine Using Anti-TB Drugs Such as Carnosine-RIF (C-HR), Carnosine-INH (C-HH), Carnosine-PYZ (C-HZ), and Carnosine-EMB (C-HE)

drug	average particle diameter (μm)	polydispersity Index	denaturation temperature °C	enthalpy ΔH(J/g)
NC	0.95	0.452	270	617.2
C−H	0.35	0.253	268.4	258.6
C-HR	2.1	0.512	243.56	511.07
C-HH	2.24	0.594	254.51	619.23
C-HZ	1.44	0.413	246.90	545.26
C-HE	0.88	0.431	257.3	682.24

H measured about 40.07 and 44.57°, respectively (Figure 4a). The spreading efficiency of the prepared formulations indicated the least hydrophobicity. Hence, the prepared C−H formulations with maximum adherence could effectively uptake anti-TB drugs, which were predominantly hydrophilic.

Figure 4b shows that the contact angle (θ) of the prepared drug formulations with RIF, INH, PYZ and EMB measured 28.81, 36.14, 47.11, and 33.78°. The θ values of C-HR, C-HH, C-HZ and C-HE were lesser compared to aqueous C−H. The results suggest that the drug composites could easily spread and wet on a clean solid surface with an angle of less than 90°. Hence, the hydrophilic composites may be solubilized in required compositions and optimized them for smooth aerosol-mediated pulmonary applications.

3.1.9. Microscopic Evaluation of Native Carnosine, Carnosine Nanoclusters and Carnosine-Anti-TB Drug Composites. The morphology of carnosine dipeptide was altered when treated with solvent (Figure 5a). In the initial experiments, the peptide nanotubes formed in HFP (C−H) are stable structures. The NC measured around ≤5−7 μm in diameter and an approximate length of around 20−50 μm, whereas in the presence of a solvent, the self-assembling process of C−H happens to form small nanostructures measuring about ≤50−100 nm in diameter and a few micrometers in length. Here, we observe that aggregations

were formed due to the formation of nanostructures. The self-assembly process in the hybrid formation influences the nanostructure arrangements. This is due to the hydrogen bonding and van der Waals force influenced by both intra- and intermolecular interactions between carnosine and anti-TB drugs. The developed hybrid drug composites have shown a distinctive variation in their morphology owing to their variation in the peptide-drug interfaces. As a result of solvent treatment, C-HR, C-HH, C-HZ, and C-HE have shown nanoorientation of arrangement as rodlike structures (Figure 5b). Noticeably, the size of the nanorods was reduced from NC and C−H. In the case of RIF, the homogeneous nanostructures were obtained with needlelike structures measuring about ∼ ≤20 nm in diameter and ∼ ≤1 μm in length. In the case of INH, fine nanorods were obtained measuring ∼10−25 nm in diameter and ∼0.5 μm in length. Obvious aggregations were obtained due to the change in the structural domain in the interaction process. PYZ nanoclusters with needlelike projections protruding upward were seen, indicating the binding of PYZ onto the carnosine backbone measuring about ≤50 nm. In the case of EMB, the drug composite exhibits an organized arrangement of nanorod-like structures owing to its hygroscopic behavior measuring about 100 nm in diameter and a few micrometers in length. It is seen from Figure 5c that carnosine could effectively carry these drugs with complex physiochemical properties and transform them into a more soluble form for maximum delivery.

3.1.10. Antimycobacterial Activity of Carnosine Nanoclusters and Carnosine-Drug Nanocomposites. In this study, we determined the in vitro antimycobacterial activity of carnosine-anti-TB drug nanocomposites against drug-sensitive *Mtb* H37Rv. The MIC values of the nanodrug composites are shown in Table 3. The MICs of RIF, INH, PYZ, and EMB were 0.25, 0.1, 200, and 10 μg/mL against *Mtb* H37Rv, whereas the MICs of carnosine- anti-TB drug nanocomposites such as C-HR, C-HH, C-HZ, and C-HE were >2, 0.025, 25, and 1.25 μg/mL, respectively. Carnosine-anti-TB drug composites showed par antimycobacterial activity against *Mtb* H37Rv when compared to conventional anti-TB drugs. MICs of C-HH, C-HZ, and C-HE exhibited significantly higher antimycobacterial activity when compared to the standard anti-TB drugs.
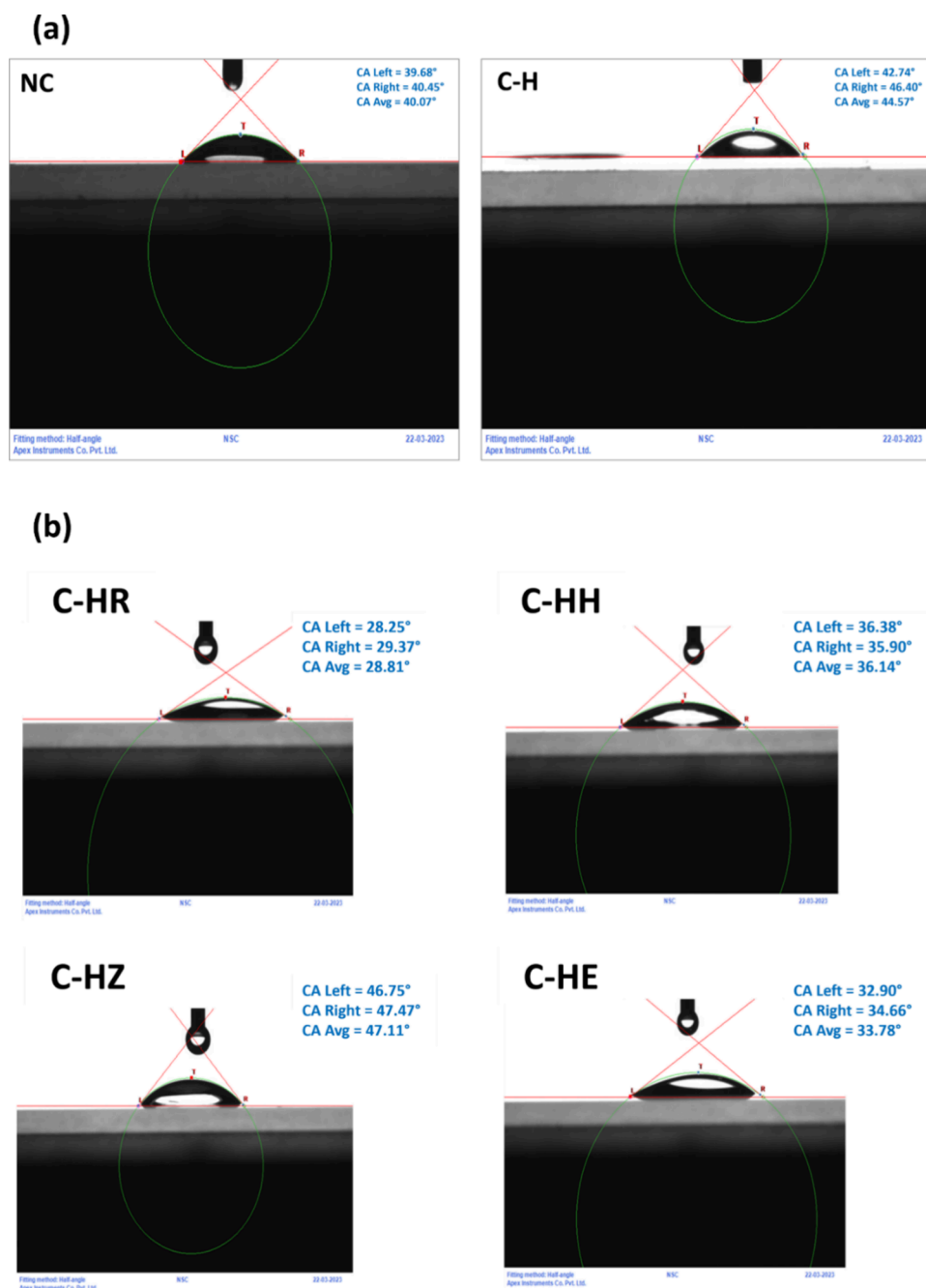
Figure 4. Contact angle measurements of (a) NC and solvent-mediated nanocarnosine (C−H) and (b) carnosine and anti-TB drug nanocomposites such as carnosine-RIF (C-HR), carnosine-INH (C-HH), carnosine-PYZ (C-HZ), and carnosine-EMB (C-HE).

It has been postulated that RIF, inhibits the DNA-dependent RNA polymerase in susceptible *Mtb* resulting in blockage of the RNA elongation. Whereas in C−R treated groups the MIC was about 2 μg/mL suggesting the sustained release of the RIF loaded onto the peptide backbone which could be exploited in controlled released therapy. Moreover, as per the literature RIF as a free molecule causes acute renal failure associated with acute interstitial nephritis.[59] Taking into account the demerits of standard RIF, the C-HR nanocomposites are formulated to reach the macrophage without any adherence and may possess a higher deposition rate that has the potential to reach the alveolar region in vivo. This assumption may be validated in our future in vivo model systems.

In the case of INH, the free form exhibited an MIC of about 0.1 μg/mL confirming the inhibition of mycolic acid production in the cell wall, whereas the carnosine anti-TB drug nanoconjugates exhibited significantly lower MIC that is 0.025 μg/mL. It indicates that a solvent-mediated process may facilitate the composites for a better drug-delivery vehicle possibly through increased cell wall adherence and membrane permeability leading to oxidative damage of DNA with apoptotic cell death. It has been shown that free INH in excess may lead to side effects such as nausea. The conjugation of anti-Tb drug with carnosine may improve drug adherence and nullify the potential adverse effects of free drugs.[60]

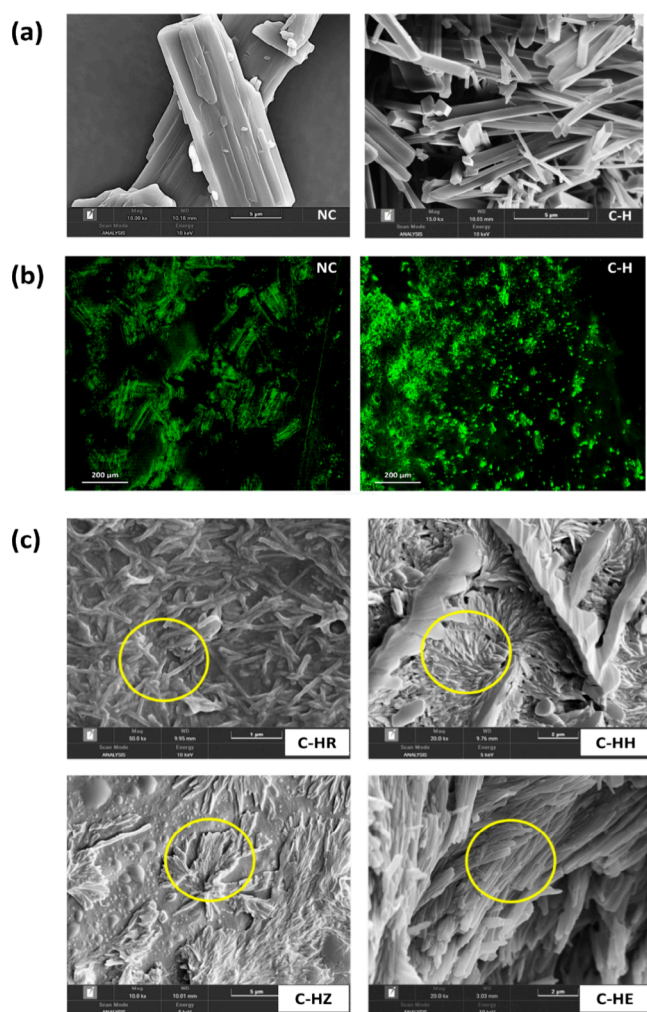PYZ inhibits the *Mtb* growth at acidic pH (pH 5−6) by promoting the accumulation of pyrazinoic acid with an MIC of

Figure 5. (a) Morphology of NC, solvent-mediated carnosine (C−H). (scale 5 μm). (b) Fluorescent microscopic image of NC and solvent-treated carnosine (C−H) (scale 50 μm). (c) Morphological analysis of carnosine-drug composite such as carnosine-RIF (C-HR), carnosine-INH (C-HH), carnosine-PYZ (C-HZ), and carnosine-EMB (C-HE) (scale 5 μm).

thereby prevents cell division. In the present study, free EMB exhibited an MIC of about 1.25 μg/mL, while the carnosine EMB nanocomposite showed an MIC of about 10 μg/mL. This may be due to the slow release profile which may be exploited for the effective deep lung delivery with minimal adverse effects. This formulation of the anti-TB drug and carnosine portrayed the importance of surface modification with an ability for minimal and sustained delivery of the drug and potential diminution of the effects of excess-free drugs. Thus, the in vitro aerodynamic behavior of the carnosine-anti-TB drug nanocomposites suggests their suitability for deep lung drug-delivery applications.

3.2. Computational Evidence of Carnosine and Anti-TB Drugs. The development of new robust strategies and evidence of scientific knowledge gaps has been assisted by vacuum studies in recent times. The computational approaches in synthetic chemistry play a major role in an animal-free approach in assessing the drug molecules for plausible use in physiological and biopharmaceutical models. Here, in this study in the field of pulmonary tuberculosis, the carnosine molecule as a novel compound needs to be analyzed for its regenerative chemical spaces with anti-TB drugs. These predictions of the iterative reaction between the dipeptide and anti-TB drug formulations can be 3D visualized and confirmed through graphical molecular models. The 2D inferences from in vitro analysis always project a knowledge deficit in explaining the mode of action of drugs and drug targets. Hence, the *Mtb* drug targets for first-line anti-TB drugs have been chosen for this study. The carnosine-anti-TB drug nanocomposites are modeled and subjected to the *Mtb* drug targets in a constraint medium, to mimic the behavior of classical anti-TB drug therapeutics. The affinity of these hybrid peptide-based anti-TB drug nanocomposites to the *Mtb* targets was studied to confirm its cellular responses to drugs, *in silico*. This observation focuses on the validation of existing results and future steps to go forward with the best practices in preclinical studies and, furthermore, for optimal therapeutic decisions.

3.2.1. Generation of Drug Conjugates through Ligand−Ligand Docking Analysis. The conjugate ligands (carnosine + anti-TB drugs) were formed upon performing ligand−ligand docking and interaction analysis with the SeamDock server. It was observed that the electronegative N and O atoms played significant roles in interaction and complex formation upon dehydration reaction as per the in vitro synthesis process. The different contributing atoms in forming conjugates and the ligand−ligand docked complex are tabulated and illustrated in Table 4 and Figure 6 respectively.

about 200 μg/mL. It is observed that the carnosine-pyrazinamide nanocomposite exhibited lesser MIC ($\sim$25 μg/mL) suggesting better activity against *Mtb* with low concentrations. This may be considered for the potential improvement in patient compliance and adverse drug effects caused by the free drug. Free EMB inhibits the arabinosyl-transferases (*embA, embB and embC*) synthesis in *Mtb* and

Table 3. MICs of Standard Anti-TB Drugs (RIF/INH/PYZ/EMB) and Carnosine-Drug Composite [Carnosine-RIF (C-HR), Carnosine-INH (C-HH), Carnosine-PYZ (C-HZ), and Carnosine-EMB (C-HE)] Using Solvent-Processed Carnosine Using Anti-TB Drugs

samples	name	stock conc. (100 μg/mL)	test conc. (μg/mL)				MIC (μg/mL)
1.	RIF	100	2	1	0.5	0.25	0.25
2.	INH	100	0.2	0.1	0.05	0.025	0.1
3.	PYZ	500	200	100	50	25	200
4.	EMB	100	10	5	2.5	1.25	10
5.	C-HR	100	2	1	0.5	0.25	>2
6.	C-HH	100	0.2	0.1	0.05	0.025	0.025
7.	C-HZ	500	200	100	50	25	25
8.	C-HE	100	10	5	2.5	1.25	1.25

Table 4. Interacting Atoms in the Formation of Carnosine-Anti-TB Conjugates

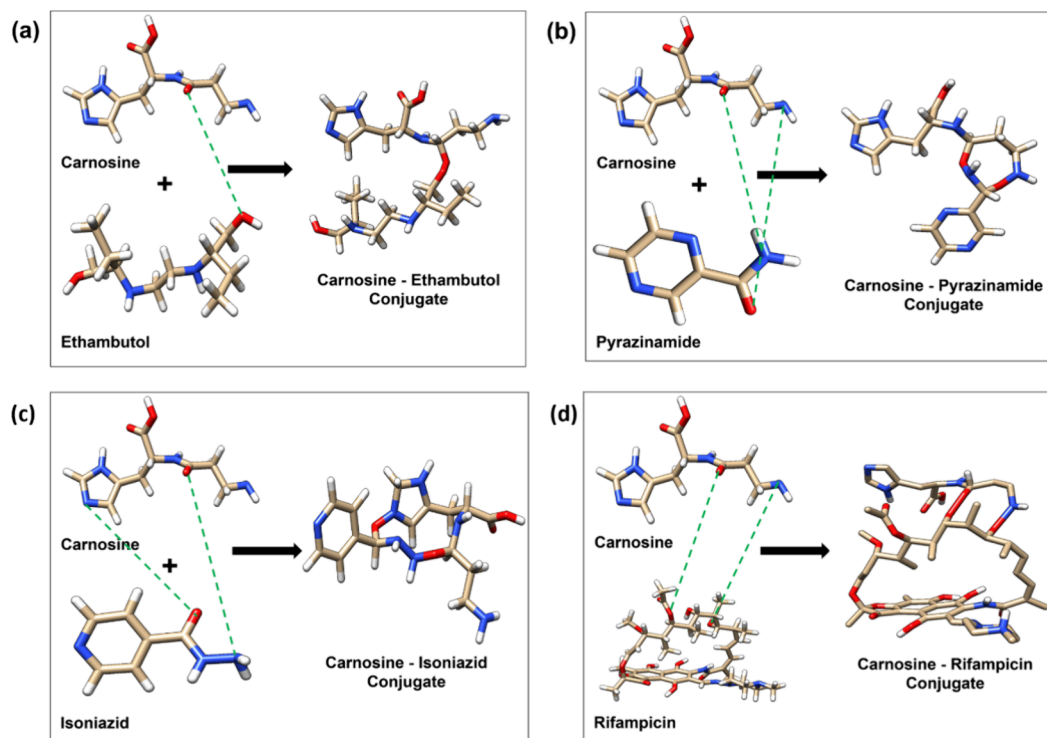| carnosine-anti-TB conjugate ligands	carnosine interacting atoms	anti-TB drug interacting atoms
Carnosine-Rifampicin	O21	O2
	N26	O3
Carnosine-Isoniazid	N3	O1
	O21	N4
Carnosine-Pyrazinamide	O21	N4
	N26	O1
Carnosine-Ethambutol	O21	O35

3.2.2. Optimization, Validation, and Active-Site Prediction of Drug Targets. The drug targets retrieved from the PDB were thoroughly scrutinized for missing residues, undesirable water molecules, and other heteroatoms. Several stretches of missing residues were detected in the loops of arabionosyl transferase EmbC (3PTY) [amino -acid residues: 795−824; 1016−1034], InhA (5VRL) [amino acid residues: 209−212], and RpoB (5ZX3) [amino acid residues: 215−225; 239−252; 323−333] proteins. Therefore, these stretches were remodeled using a homology-based modeling approach, considering their parent protein as the template. Thereafter, the modeled structures were subjected to superimposition analysis as depicted in Figure 1. The modeled stretches were cured upon formation of loops, and the relative RMSD explained that the structures did not deviate much (<5 Å) from the parent proteins.

Thereafter, all target proteins were subjected to tertiary structural validations to estimate their gross and local erroneous zones. The global model quality estimated from the Z-score ProSA-web revealed that all four target proteins 3PTY (−5.21), 4NNI (5.55), 5VRL (−8.14), and 5ZX3 (−14.76) were well positioned within the experimentally validated protein structures, revealing minimal gross errors in the structure. Further, the energetics from the ProSA-web revealed the energy functions tagged to each amino acid residue. From Figure S2, it can be deduced that all of the studied proteins laid well below the threshold cutoff of 0.0, signifying minimal steric hindrance in protein folding and minimal erroneous conformation glitches. The spatial orientations and bond metrics were further calculated upon Ramachandran plot analysis which revealed that 99.6, 100, 98.7, and 100% of residues from 3PTY, 4NNI, 5VRL, and 5ZX3, respectively. were well positioned in the allowed and favorable zones (Figure S2).

The active site or catalytic domain analysis from InterPro and Pfam revealed that the active site or EMB drug-binding site in 3PTY lies in arabinosyltransferase (EmbC) C-terminal domain (amino acid residues: 720−1092) [IPR032731, PF14896], while for 4NNI, the active site for PYZ lies in the nucleic acid binding domain (amino acid residues: 278−268) of ribosomal protein S1 [IPR012340]. INH binds to the InhA protein upon interacting with the enoyl-[acyl-carrier-protein] reductase (NADH) [IPR0143358] and NAD(P)-binding-domain-superfamily domain [IPR036291] present within amino acid residues 2−269. The active site for RpoB (5ZX3), the target for RIF, lies in the DNA-directed RNA polymerase β-subunit [IPR010243] spanning between the amino acid residues of 39−1140.

3.2.3. Molecular Docking and Intermolecular Interaction Analysis. Molecular docking of putative *Mtb* drug targets with classical anti-TB drugs (positive control), carnosine (negative control), and carnosine-anti-TB conjugates (test) was performed to testify the binding affinity and inhibition constants between them (Figure 7). It was evident from the

Figure 6. Formation of carnosine-anti-TB conjugates: (a) Carnosine-EMB (C-HE) conjugate, (b) carnosine-PYZ (C-HZ) conjugate, (c) carnosine-INH (C-HH) conjugate, and (d) carnosine-RIF (C-HR) conjugate.
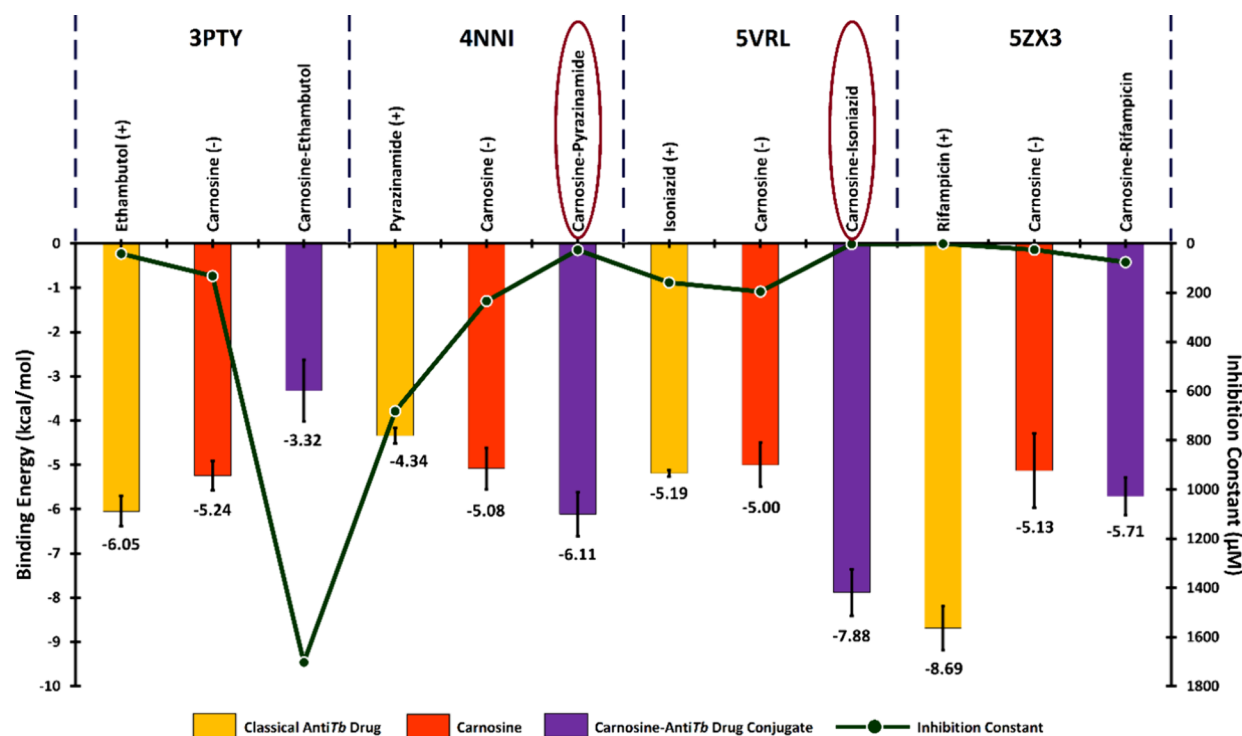
Figure 7. Binding energies and inhibition constants of classical anti-TB drugs, carnosine, and carnosine-anti-TB conjugates with 3PTY, 4NNI, 5VRL, and 5ZX3.

binding scores that the 3PTY-EMB (-6.05 ± 0.34 kcal/mol) and 5ZX3-RIF (-8.69 ± 0.5 kcal/mol) complexes have better binding affinities when compared to C-HE (-3.32 ± 0.7 kcal/mol) and C-HR (-5.71 ± 0.42 kcal/mol) conjugates complexed with 3PTY and 5ZX3, respectively. On the contrary, the conjugates of C-HZ (-6.11 ± 0.5 kcal/mol) and C-HH (-7.88 ± 0.53 kcal/mol) complexed with 4NNI and 5VRL, respectively, displayed lower binding energy and high binding affinity when compared to their classical pair of 4NNI-PYZ (-4.34 ± 0.18 kcal/mol) and 5VRL-INH (-5.19 ± 0.07 kcal/mol) complexes, respectively. Subsequently, there is a drastic decrease in the inhibition constant of C-HZ (25.85 μM) and C-HH (2.28 μM) complexes as compared to their classical counterpart of 681.23 and 158.23 μM for PYZ and INH alone. Though NC had an average binding energy of $\sim$ -5.11 ± 0.54 kcal/mol and an inhibition constant of $\sim$146.77 μM with all four drug targets, it does not reflect in in vitro antimycobacterial effects. Therefore, carnosine could be used only as a potential drug-delivery vehicle as evident from our present and previous studies, which facilitates better binding attributes as evident from C-HZ and C-HH complexes.

Intermolecular interaction analysis of these studied complexes revealed that all of the studied drugs bound to the arabinosyltransferase (EmbC) C-terminal domain. EMB established 5 H bonds with the polar residues (E924, K927, D1017) and several van der Waals (A801, A1020, Y922, and G923), alkyl, π-alkyl (I802, Y1018), and C−H bonds (P926) (Figure 8a), while carnosine established two hydrogen bonds with D869 and L865 besides van der Waals (P866), C−H, and π-alkyl (P868, K867) interactions (Figure 8b). The conjugate C-HE established six H bonds with the polar residues (D869, L971, and D870), C−H bonds (D970), and several van der Waals interactions (A761, D758, R972, E756, P757, and P868) (Figure 8c). It was evident that all three protein−ligand

complexes got bound to the pocket comprising the active-site residues as mentioned with a drug-binding score ranging from 0.66 to 0.99. The classical drug PYZ and the C-HZ conjugate interacted with the nucleic acid binding domain (IPR012340). The classical anti-TB drug established three H bonds with the active residues I323, A327, and polar H330 which were also involved in π-sulfur interactions. The complex was further stabilized by several van der Waals and π-alkyl interactions (Figure 8d). Carnosine displayed better intermolecular interactions with 4NNI as evidenced by the better binding affinity of -5.08 kcal/mol compared with PYZ (-4.34 kcal/mol). Carnosine displayed six H bonds with E315 and R423 while displaying several stabilizing π-alkyl and van der Waals interactions (Figure 8e). The C-HZ conjugate displayed nine H bonds with the active polar residues of A299, R312, E314, E315, A344, and R423 besides establishing π-cation/anion (D343 and R423), π-alkyl (P298 and M427), and several van der Waals (K300, V313, and E420) interactions (Figure 8f). All these complexes got bound to the active-site pockets as predicted from the Pock Drug server with drug-binding scores ranging between 0.5 and 0.7.

The drug moieties INH and C-HH conjugate interacted with the enoyl (NADH) [IPR0143358] and NAD(P) binding [IPR036291] domains. The classical anti-TB drug INH displayed three H bonds (T51 and A58) alongside several stabilizing interactions from C−H (L54), π-alkyl (K57), and van der Waals (L38, D52, A56, L60) interactions (Figure 8g). The negative control carnosine also displayed five H bonds (D64, L63, and G14) alongside several stabilizing interactions from van der Waals and π-sigma (I95) interactions (Figure 8h). The C-HH complex displayed multiple interactions with the active residues forming four H bonds (D64 and T39), π-alkyl (V65), π-sigma (I95), and π-lone pairs (L63) and several van der Waals interactions with the polar residues (Figure 8i).
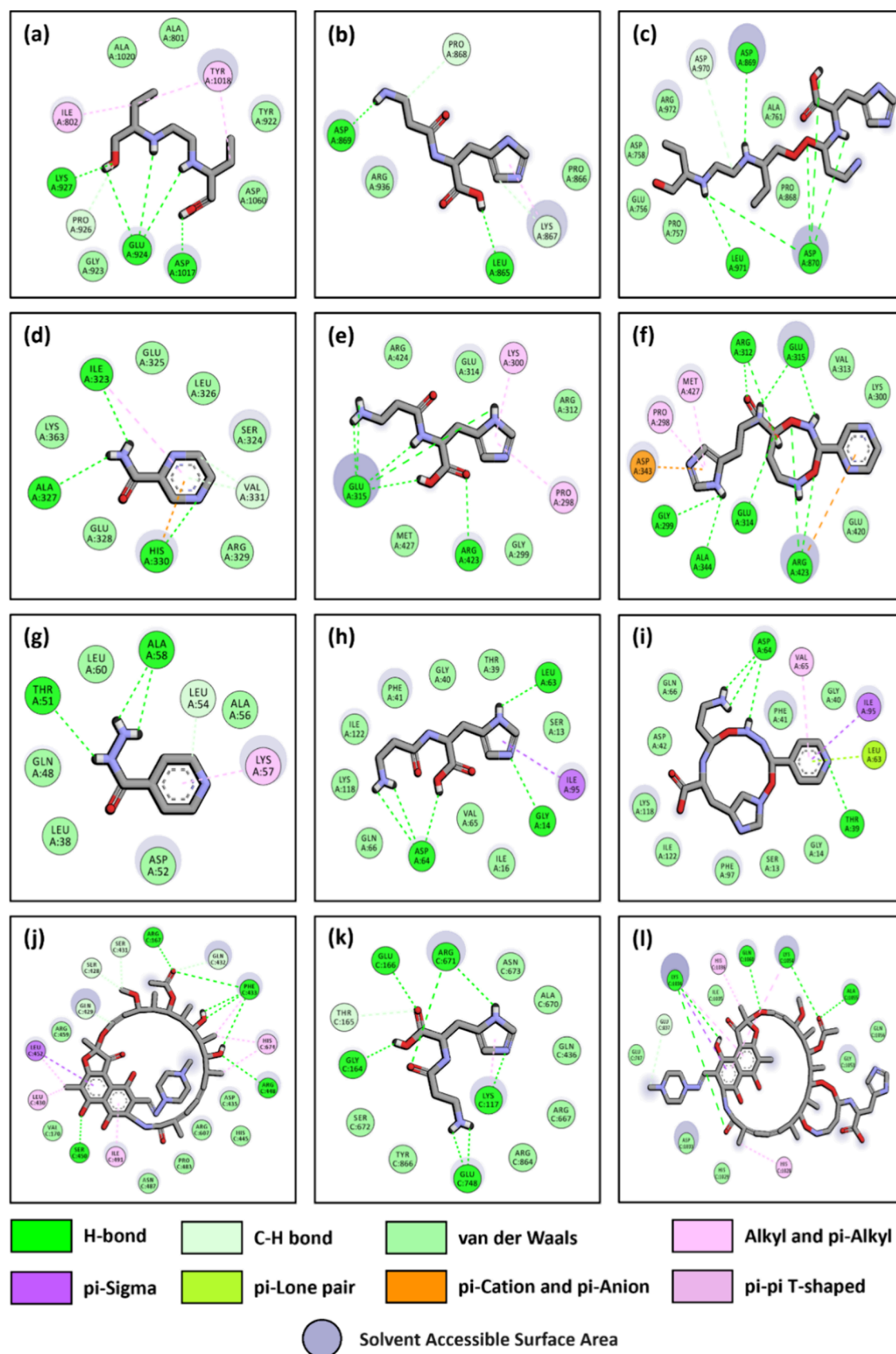
Figure 8. Intermolecular interaction analysis of (a) 3PTY-EMB complex, (b) 3PTY-carnosine complex, (c) 3PTY-carnosine-EMB (C-HE) complex, (d) 4NNI-PYZ complex, (e) 4NNI-carnosine complex, (f) 4NNI-carnosine-PYZ (C-HZ) complex (g) 5VRL-INH complex, (h) 5VRL-carnosine complex, (i) 5VRL-carnosine-INH (C-HH) complex, (j) 5ZX3-RIF complex, (k) 5ZX3-carnosine complex, and (l) 5ZX3-carnosine-RIF (C-HR) complex.

Table 5. Second-Order Perturbation Theory Analysis of Fock Matrix in NBO Basis[a]

donor NBO (i)		acceptor NBO (j)		$E^{(2)}$ (kcal/mol)	$E(j) - E(i)$ (a.u.)	$F(i,j)$ (a.u.)
bond/lone pair	atoms	antibonding bond	atoms			
Isoniazid						
LP (1)	N2	BD* (2)	C8	42.98	0.33	0.107
LP (2)	O1	BD* (1)	C8	27.37	0.68	0.124
BD (2)	C5−C7	BD* (2)	N3−C10	26.56	0.27	0.076
BD (2)	N3−C10	BD* (2)	C6−C9	25.00	0.33	0.081
BD (2)	C6−C9	BD* (2)	C5−C7	23.45	0.28	0.073
Carnosine-Isoniazid						
LP (2)	O14	BD* (2)	C12−O13	43.99	0.35	0.112
LP (2)	O13	BD* (1)	C12−O14	33.67	0.61	0.13
BD (2)	C31−C33	BD* (2)	N29−C30	28.03	0.27	0.078
BD (2)	N29−C30	BD* (2)	C28−C35	25.94	0.32	0.082
BD (2)	C28−C35	BD* (2)	C31−C33	23.99	0.28	0.074
Pyrazinamide						
LP (1)	LP (1)	LP (1)	LP (1)	LP (1)	LP (1)	LP (1)
BD (2)	BD (2)	BD (2)	BD (2)	BD (2)	BD (2)	BD (2)
LP (2)	LP (2)	LP (2)	LP (2)	LP (2)	LP (2)	LP (2)
BD (2)	BD (2)	BD (2)	BD (2)	BD (2)	BD (2)	BD (2)
BD (2)	BD (2)	BD (2)	BD (2)	BD (2)	BD (2)	BD (2)
Carnosine-Pyrazinamide						
LP (1)	LP (1)	LP (1)	LP (1)	LP (1)	LP (1)	LP (1)
LP (1)	LP (1)	LP (1)	LP (1)	LP (1)	LP (1)	LP (1)
BD (2)	BD (2)	BD (2)	BD (2)	BD (2)	BD (2)	BD (2)
BD (2)	BD (2)	BD (2)	BD (2)	BD (2)	BD (2)	BD (2)
LP (1)	LP (1)	LP (1)	LP (1)	LP (1)	LP (1)	LP (1)

[a]LP, lone pair; BD, bond pair; *, antibonding; $E^{(2)}$, energy of hyper conjugative interaction (stabilization energy); $E(j) - E(i)$, Energy difference between donor and acceptor NBO orbitals; $F(i,j)$, Fock matrix element between i and j NBO orbitals.

Similarly, the three ligands got bound to 5VRL upon interacting with the active-site residues within the active groove with the drug score ranging from 0.96 to 0.99. The standard drug for the treatment of tuberculosis, RIF, displayed the best binding affinity compared to all of the studied ligands used in the study. It was evident from the intermolecular interaction patterns displayed by RIF that showed a wide array of bonding with the active residues of the DNA-directed RNA polymerase β-subunit [IPR010243]. RIF interacted with seven H bonds (R167, F433, and S450), two C−H bonds (S428 and S431), six alkyl and π-alkyl (L430, I491, and H674) interactions beside π-sigma (L452) and several van der Waals interactions with the polar amino acid residues which comprise the active groove of the drug target (Figure 8j). Carnosine also displayed similar intermolecular interactions inside the active groove displaying seven H bonds (E166, R671, K117, E748, and G164), C−H bond (T165), π-alkyl (K117), and several stabilizing van der Waals interactions but with a much feeble binding affinity of −5.13 kcal/mol when compared to that of RIF (−8.69 kcal/mol) (Figure 8k). The C-HR conjugate also establishes several interactions in the form of H bonds (K1034, Q1060, K1054, and A1055), alkyl and π-alkyl (K1034, H1036, K1054, and H1028), π-sigma (K1034), and several stabilizing van der Waals interactions (Figure 8l). RIF, carnosine, and C-HR conjugate were observed to bind to the RNA polymerase β subunit in multiple poses and orientations, however, interacting with the active domain, and groove with the drug score ranging within 0.76−1.00.

From the binding energies, inhibition constants, and intermolecular interaction patterns, it is evident that the classical anti-TB drug, carnosine, and carnosine-anti-TB

conjugate interacted with the key residues of the active/catalytic domains of their respective protein targets, which had high drug-binding probability. Moreover, the C-HZ and C-HH conjugates proved to have better binding affinity and intermolecular interactions, as revealed from the docked poses. However, RIF and EMB displayed better interaction and binding affinities alone than those in conjugates. From the docked poses, it can be further deciphered that the electronegative O- and N atoms and the π-electrons from the aromatic ring structures played effective roles in contributing majorly to the H-bonding, π-alkyl, π-sigma, π-cation/anion, and π−π interactions. Therefore, it can be hypothesized that the resonating π electrons and the lone pairs of electronegative O and N atoms are crucial sites for causing nucleophilic attacks with the active residues of the target. Since the C-HZ and C-HH conjugates displayed better binding profiles with the target, they were further subjected to quantum chemical simulations through density functional theory calculations to decipher their enhanced reactivity patterns compared to those of the classical counterparts when tested alone.

3.2.4. Ligand Structure Optimizations and Assessments of Reactivity Parameters. The classical anti-TB drug PYZ was composed of 14 atoms and 64 electrons, while INH consisted of 17 atoms and 72 electrons. The conjugates C-HZ consisted of 44 atoms and 184 electrons, while C-HH possessed 49 atoms and 194 electrons. The ligand structure optimizations were achieved upon performing density functional theory simulations under the B3LYP/6-311G++(d,p) basis set. The conjugates were compared with their lone classical counterparts to decipher their enhanced reactivity and stability parameters. The optimized bond lengths (Å), bond angles
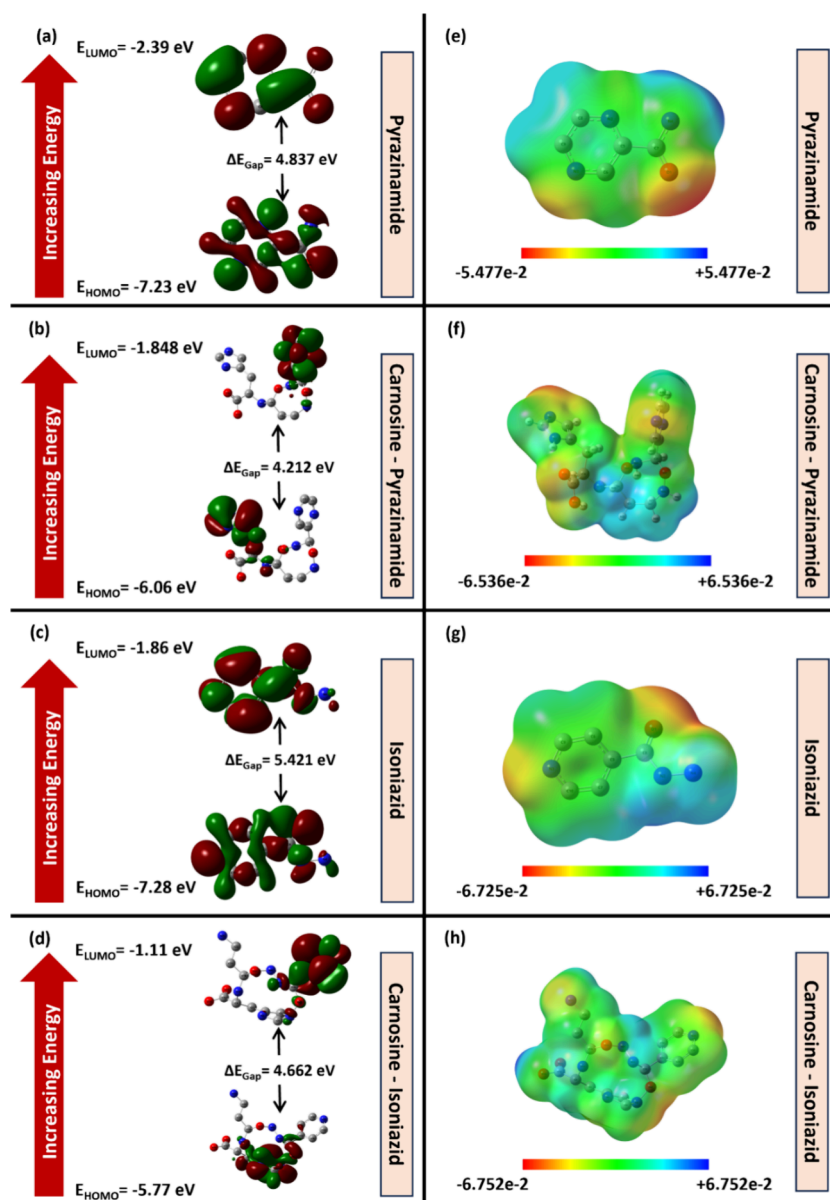
Figure 9. FMOs highlighting the HOMO−LUMO map of (a) pyrazinamide, (b) carnosine-pyrazinamide (C-HZ), (c) isoniazid, and (d) carnosine-isoniazid (C-HH). MEP of (e) pyrazinamide, (f) carnosine-pyrazinamide (C-HZ), (g) isoniazid, and (h) carnosine-isoniazid (C-HH).

(°), and dihedral angles (°) of all studied leads and their optimizations were confirmed from their minimized energy profiles, and their structures with the atom numbering scheme are illustrated in Figure S3.

3.2.5. NBO Analysis. The reactivity of the molecule depends on the charge delocalization due to electronic transitions from bonding to antibonding orbitals which is studied through the NBO analysis. From the present study, it could be understood that the transition of lone pairs from the electronegative O and N atoms played a major role in providing stability to the lead molecules. The five major electronic transitions that stabilized the studied leads are tabulated in Table 5.

In PYZ, the highest contribution to stabilize the molecule was observed from the electronic transition of LP (N4) → π^* (O1−C7), followed by BD (N3−C9) → π^* (C5−C6) and LP (O1) → π^* (N4−C7) with stabilizing energies of 63.92, 24.75, and 24.32 kcal/mol, respectively, while the conjugate C-HZ was majorly stabilized by the transition of LP (C31) → π^*

(N34−C36) followed by LP (C31) → π^* (N29−C30) and BD (N34−C36) → LP* (C32) with stabilizing energies of 82.51, 76.41, and 54.82 kcal/mol, respectively. Simultaneously, INH molecule was greatly stabilized due to the electronic transition of LP (N2) → π^* (C8) followed by LP (O1) → π^* (C8) and BD (C5−C7) → π^* (N3−C10) with stabilizing energies of 42.98 37.37, and 226.56 kcal/mol, respectively, while the conjugate C-HH was stabilized due to the electronic transition of LP (O14) → π^* (C12−C13) followed by LP (O13) → π^* (C12−O14) and BD (C31−C33) → π^* (N29−C30) with stabilizing energies of 43.99, 33.67, and 28.03 kcal/mol, respectively. In both the cases of E(2) stabilization energies, it is revealed that the carnosine-anti-TB conjugate pairs C-HZ (63.92 kcal/mol) and C-HH (43.99 kcal/mol) were better stabilized than their lone classical counterparts. This could be a reason for their enhanced reactivity as evident from their increased binding affinities with 4NNI and 5VRL. The NBO profiles are further understood and validated with

Table 6. Global Reactivity Parameters for Isoniazid and Pyrazinamide Compared with Their Conjugate with Carnosine[a]

global descriptors	isoniazid (eV)	carnosine-isoniazid (eV)	pyrazinamide (eV)	carnosine-pyrazinamide (eV)
E_{HOMO}	−7.283	−5.773	−7.229	−6.06
E_{LUMO}	−1.862	−1.111	−2.392	−1.848
Energy Gap (ΔE)	5.421	4.662	4.837	4.212
Ionization Energy (I)	7.283	5.773	7.229	6.06
Electron Affinity (A)	1.862	1.111	2.392	1.848
Electronegativity (χ)	4.573	3.442	4.811	3.954
Chemical Potential (ρ)	−4.573	−3.442	−4.811	−3.954
Chemical Hardness (η)	2.7105	2.331	2.4185	2.106
Chemical Softness (δ)	0.369 eV^{-1}	0.429 eV^{-1}	0.414 eV^{-1}	0.475 eV^{-1}

[a]HOMO, highest occupied molecular orbital; LUMO, lowest unoccupied molecular orbital.

FMO analysis, which explains the shifting of the electron cloud from HOMO to LUMO. The HOMO−LUMO profile further explains the reactivity and global reactivity metrics of the studied inhibitors.

3.2.6. FMO Analysis. HOMO represents the filled orbitals or orbitals with lone pairs, while LUMO represents vacant degenerate orbitals. The energy gap (ΔE) represents the energy required for the electronic transition from HOMO to LUMO which governs the molecular stability and reactivity profiles concerning the electronic, chemical, and optical properties of the studied molecule. From the HOMO−LUMO transition maps, it can be observed that there is a clear transition of the electronic cloud from the bonding orbitals of HOMO to antibonding LUMO in the conjugates (Figure 9a−d). In the C-HZ conjugate, the HOMO electron cloud over the cyclic ring C1−N2−C3−C5-N6 and N9 shifts to resonating LUMO electron cloud comprising cyclic N29−C30−C31−C32−N34−C36 atoms. Similarly, in the C-HH complex, the HOMO−LUMO electronic cloud transition occurs as electrons shift from cyclic C1−C2−N3−C4−N5 and C8 atomic centres and C38−O42 atomic centres to the resonating LUMO cloud comprising C28−N29−C30−C31−C33 atomic centers. The HOMO−LUMO profile further validates the NBO analysis as the electronic transition stabilizing the molecule contemplates the LUMO transitions in both C-HZ and C-HH conjugates.

3.2.7. Global Descriptor Analysis. The HOMO−LUMO profile and energy gap are pivotal to assessing the chemical reactivity or inertness of the studied inhibitors. The vital parameters to understand the global reactivity descriptors of the molecule are tabulated in Table 6. From Table 6, it is evident that the conjugate ligands, namely, C-HZ (4.212 eV) and C-HH (4.662 eV), scored less than the lone classical drugs, PYZ (4.837 eV) and INH (5.421 eV). Similarly, the ionization energies of both C-HZ (6.06 eV) and C-HH (5.773 eV) are lower than those of their classical drugs. Both these parameters reflect that the C-HZ and C-HH conjugates will display high reactivity profiles. Upon studying the chemical potential, chemical hardness, and chemical softness profiles, it is observed that both the conjugates C-HZ (−3.954 eV, 2.106 eV, 0.475 eV^{-1}) and C-HH (−3.442 eV, 2.331 eV, 0.429 eV^{-1}) scored high chemical potential, low chemical harness, and high chemical softness profile, respectively, signifying that the conjugates are electrophilic and will effectively undergo electrophilic addition/substitution reaction. Therefore, the FMO analysis validates the NBO electronic transition profiles which explain the high reactivity profiles of the conjugate ligands. Therefore, it can be deduced that carnosine facilitates

the enhanced reactivity profiles and could be used as an alternative to treating with classical drugs alone.

3.2.8. MEP Analysis. MEP maps provide crucial leads to understanding the chemical reactivity of the molecule upon analyzing the electropositive and electronegative centers. These centers provide pivotal roles in establishing chemical bonds upon interacting with their drug targets as evident from the intermolecular interaction profiles. In the current study, the MEP was mapped over electrostatic potential under the B3LYP/6-311G + + (d,p) basis set of theory where the red and blue colored zones indicate sites of nucleophilic and electrophilic attacks only. MEP profiles are global descriptors indicating that the conjugates are good electrophilically as evident from the blue-green coloration on the MEP maps (Figure 9e−h). From the intermolecular interaction profiles and MEP maps, it is observed in C-HZ complexes that the electropositive centers established interactions mainly with the negatively charged acidic amino acids like H bonds with E314, π-sulfur bonds with D343, and van der Waals interactions E420 and E315, while mildly electronegative O16 established a H bond with R312. On the other hand, sparse interactions were established by PYZ alone. Being less electropositive as compared to its conjugate, the electronegative center N3 made an H-bond interaction with the positively charged H330, while van der Waals interactions were observed between electronegative O1 with K363 and N3 with R329.

Upon correlating the intermolecular interaction profile and MEP map of C-HH, it could be understood that the electropositive centers of the ligand formed H-bond interaction with the negatively charged acidic amino acid residues D64 and van der Waals interaction between O15 and D42 apart from several other interactions, while relatively more electronegative ligand INH established nucleophilic attacks between electronegative N3 and positively charged K57. Therefore, from the above analyses, the underlying reasons of enhanced reactivity displayed by the C-HZ and C-HH conjugates can be clearly understood, and so the current study identifies them as better alternatives than administration of the classical drugs alone.

3.2.9. Stability Analysis of Carnosine-Anti-TB Drug Conjugates through MDSs. C-HZ and C-HH displayed better binding efficacy and enhanced reactivity parameters as they effectively interacted with the crucial amino acid residues of their respective targets. Therefore, these two drugs were further subjected to MDS analysis, and their trajectories were compared with their classical anti-TB counter drugs. The RMSD profile concerning the protein backbone of PYZ upon reacting with 4NNI was recorded to be 0.23 ± 0.04 nm, while C-HZ got stabilized at a lower average RMSD of 0.21 ± 0.03
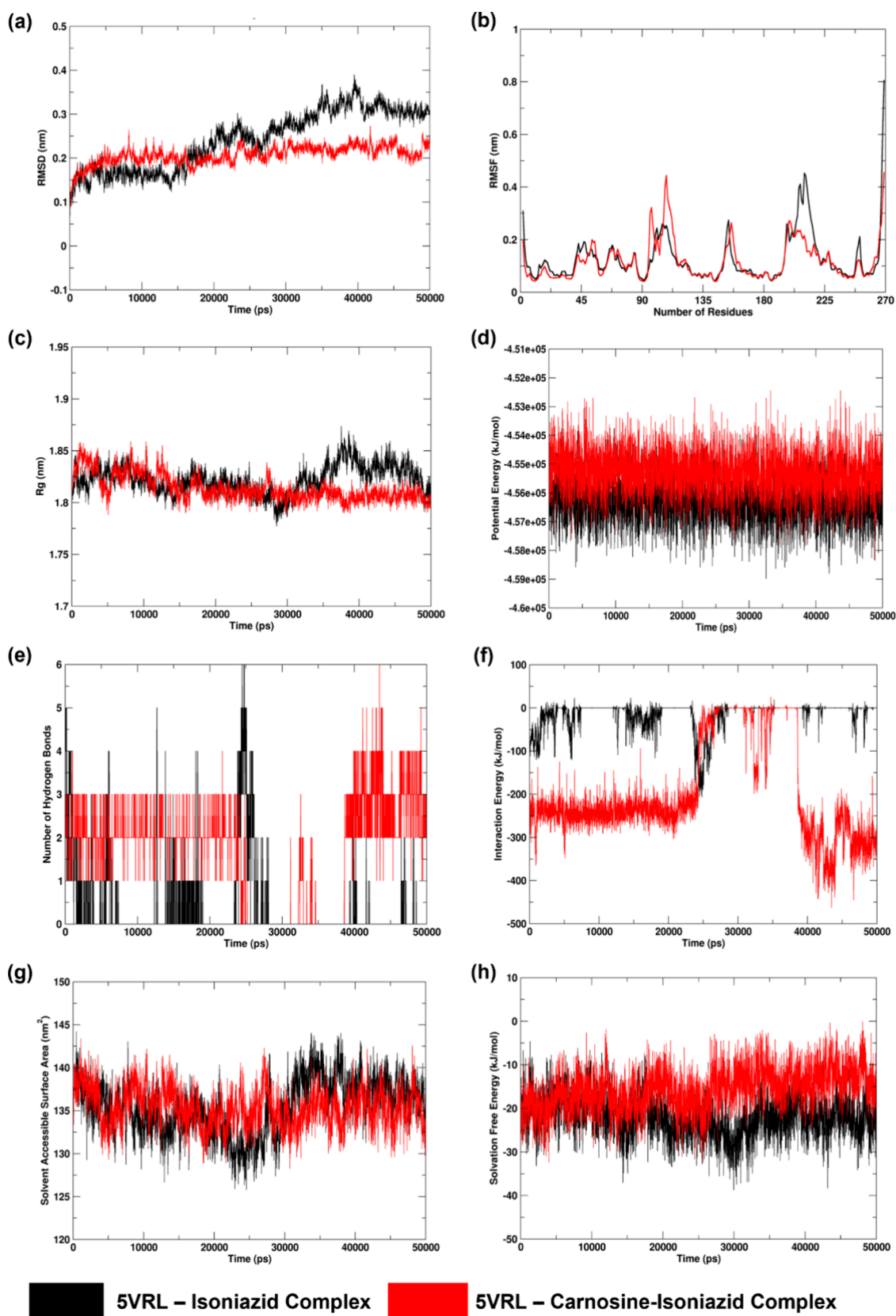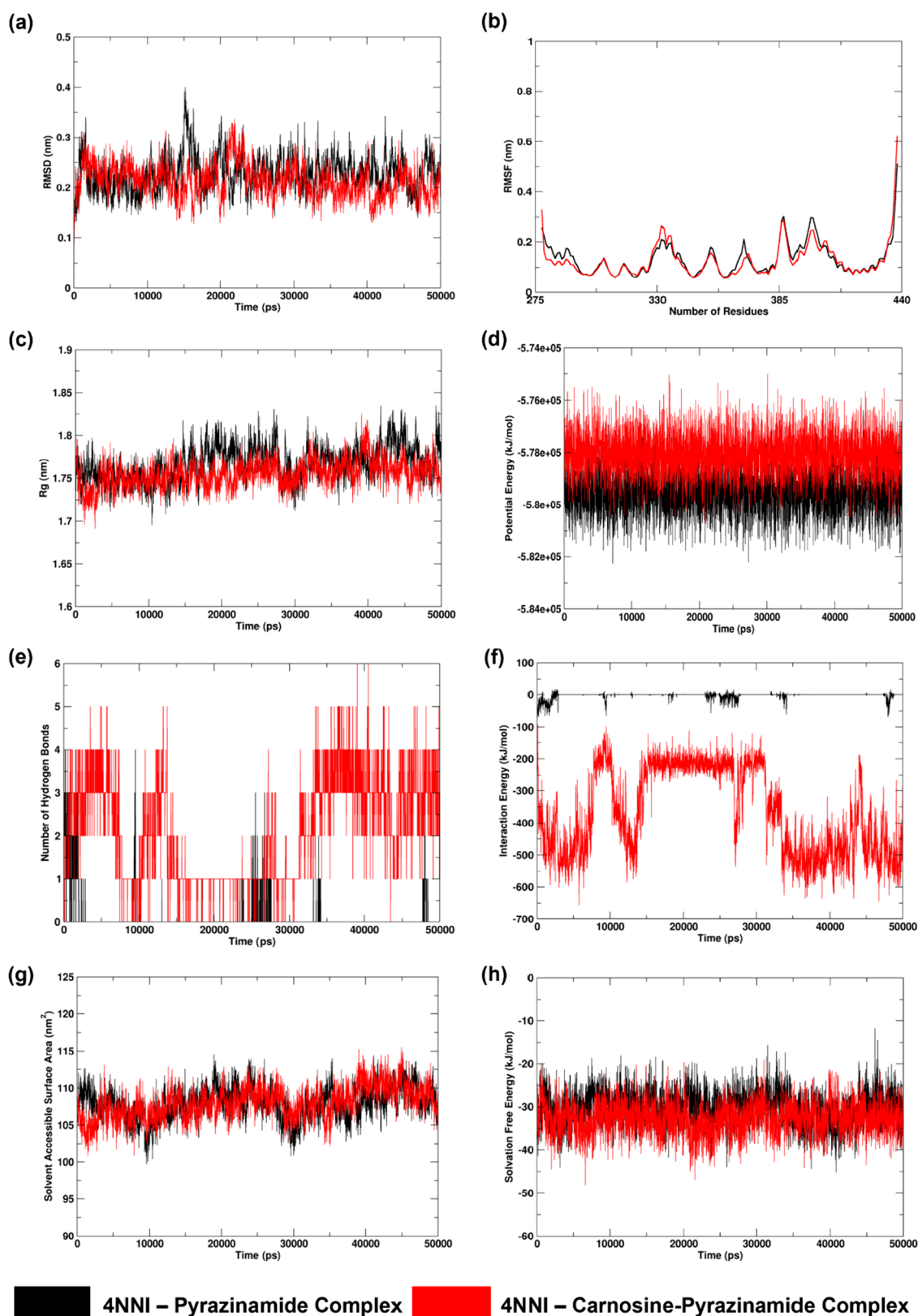
Figure 10. MDS profiles of 4NNI complexed with pyrazinamide and carnosine-pyrazinamide (C-HZ). (a) RMSD curve. (b) RMSF plot. (c) Rg trajectory. (d) Potential energy. (e) Number of intermolecular (protein–inhibitor) hydrogen bonds. (f) Interaction energy profile. (g) SASA trajectory. (h) Free energy of solvation.

nm. Though both the complexes displayed stable trajectories which were maintained throughout the studied time frame, the

C-HZ conjugate had lesser deviations when compared to its control (Figure 10a). While assessing the residual-level

Figure 11. MDS profiles of 5VRL complexed with isoniazid and carnosine-isoniazid (C-HH). (a) RMSD curve. (b) RMSF plot. (c) Rg trajectory. (d) Potential energy. (e) Number of intermolecular (protein-inhibitor) hydrogen bonds. (f) Interaction energy profile. (g) SASA trajectory. (h) Free energy of solvation.

fluctuations of both PYZ (0.13 ± 0.04 nm) and C-HZ (0.13 ± 0.07 nm), there were not many fluctuations that were recorded in both cases, which indicates that the inclusion of relatively

bulky ligands had no impact of the orientation of the active groove or protein conformation (Figure 10b). The compactness of the complexes as determined from the Rg trajectories

indicated that the complex formed with the C-HZ (1.75 ± 0.01 nm) conjugate would display less steric hindrance and minimal spatial distortions though there was not much variation when compared to the 4NNI-PYZ (1.77 ± 0.02 nm) complex. From Figure 10c, it could be seen that the conjugate displayed a better stability curve with minimal deviations as compared to PYZ alone. However, both 4NNI-PYZ and 4NNI with C-HZ complexes maintained the potential energy profiles at a constant $-5.795 \times 10^{+05}$ and $-5.780 \times 10^{+05}$ kJ/mol, respectively (Figure 10d). The H-bond analysis validates the intermolecular interaction profile obtained from molecular docking studies, which revealed that C-HZ consistently interacted with ∼4−6 H bonds, while only 1−2 H bonds were seen in the 4NNI-PYZ complex (Figure 10e). This sparse interaction pattern of the 4NNI-PYZ complex can be better understood from the interaction energy profile with minimal −8.16 kJ/mol, while the C-HZ conjugate interacted with 4NNI with an energy of −359.68 kJ/mol (Figure 10f). The disruption in the H bonds in the 4NNI-PYZ complex can also be observed throughout while there was not much disruption in the 4NNI-C-HZ complex. Both 4NNI-PYZ and 4NNI-C-HZ complexes achieved a uniform layer of solvation as understood from the SASA (107.92 ± 2.15 and 107.98 ± 2.2 nm^2) and free energy of solvation (−30.16 ± 3.9 and −32.69 ± 3.78 kJ/mol), respectively (Figure 10g,h).

On equating the 5VRL complexed with INH and C-HH conjugate, it was observed that the conjugate stabilized at a lower RMSD score of 0.21 ± 0.02 nm concerning the backbone atoms, while INH had slightly higher RMSD of 0.24 ± 0.07 nm. From the trajectory curve, it was also evident that the conjugate displayed a stable profile throughout the studied time frame, while 5VRL-INH had shown increased fluctuation after the 15,000 ps time frame and maintained a higher trajectory thereafter (Figure 11a). However, there was not much deviation in the residue-level fluctuations as both the 5VRL-INH (0.13 ± 0.09 nm) and 5VRL-C-HH (0.12 ± 0.07 nm) complexes, signifying that the drug target did not experience much distortion upon integrating the inhibitor molecule inside its active groove (Figure 11b). The compactness indicating the folding distortions in the complex revealed that the Rg of the complex with the conjugate ligand (1.81 ± 0.01 nm) decreased with the time frame while there was an increment of Rg (1.82 ± 0.01 nm) after 25,000 ps in 5VRL-INH complex. This indicates that the 5VRL-C-HH complex being more compact harbors minimal gross and local erroneous folds, therefore less steric hindrance and more stability (Figure 11c). However, both 5VRL-INH ($-4.562 \times 10^{+05}$ kJ/mol) and 5VRL-C-HH ($-4.552 \times 10^{+05}$ kJ/mol) complexes maintained uniform levels of potential energy indicating proper equilibration of the simulated systems (Figure 11d). Similar to the previous conjugate complex, H-bond analysis of the C-HH complex too validated the intermolecular interactions from the docking analysis, indicating an average of 3−4 stable H bonds which was maintained throughout the simulation time frame, while the INH could establish 1−2 stable H bonds with 5VRL (Figure 11e). The H-bond interaction pattern could be better understood from the interaction energy profile, where 5VRL-INH (−26.00 kJ/mol) scored much less compared to the 5VRL-C-HH (−235.84 kJ/mol). Moreover, there was much discontinuity in the interaction energy profile of 5VRL-INH indicating lesser affinity of the drug under dynamic conditions, whereas there were dense interaction regions in the 5VRL-C-HH interaction

energy plot, meaning the conjugate has better binding affinity with its target (Figure 11f). Though both 5VRL-INH and 5VRL-C-HH complexes revealed similar SASA energy profiles of 135.41 ± 3.14 and 135.34 ± 2.32 nm^2 and free energy of solvation of −21.80 ± 4.7 and −15.65 ± 4.93 kJ/mol the 5VRL-C-HH complex displayed better trajectories with minimal fluctuations (Figure 11g,h). Therefore, from the above MDS scores and trajectories of both the 4NNI-C-HZ and 5VRL-C-HH complexes, it can be elucidated that these conjugates had better interaction profiles with their respective targets and, therefore, indicate better stabilities than 4NNI-PYZ and 5VRL-INH complexes.

The formulated nanocomposites (C-HR, C-HH, C-HZ, and C-HE) were screened against H37Rv *Mtb* in in vitro standard procedures. In comparison with classical drugs (RIF/INH/ PYZ and EMB), the antimycobacterial effect of formulated nanocomposites projects an inhibition effect against *Mtb* except for RIF. Despite this, the process seems insufficient to support the peptide-linked anti-TB drug mechanism of action in the host bacterium. Hence, the allosteric effects and binding pockets of carnosine-anti-TB drug nanocomposites in the *Mtb* targets were located through a molecular dynamics approach. Remarkably, both in vitro and *in silico* approach results correlated with each other. It is observed that the C−CH and C-HZ nanocomposites have shown better inhibition toward *Mtb* drug targets with maximum binding efficiency.

In recent times, as an evolution of nanotechnology, researchers have functionalized nanomaterials to act as a platform for specific activity, localization, sustained release, and targeted delivery.[61] Here, carnosine nanocomposites with compatible physicochemical and biological parameters could be excellent substrates for cell manipulation, immune cell targeting, and reversing microbial attack. Moreover, in future, these carnosine nanocomposites can be used to create a three-dimensional microenvironment to monitor the response of *Mtb* and its symptoms.

4. CONCLUSIONS

The intervention of modern technology like nanotechnology in therapeutic drug delivery plays a significant role in the size reduction of biomacromolecules. The size control and morphology were found to be of significant interest to enhance additional functions like site-specific behavior, drug-loading mechanism, and release profile. The present study describes the development of carnosine nanoclusters through a solvent-mediated process with an average diameter of >50 nm and carnosine-anti-TB drug composites of size less than <1.5 μm. The solvent-mediated approach has influenced spectral properties, and the findings gain information on the physical, chemical, and morphological significance for pulmonary delivery. Reduced enthalpy of the nanocomposites confirms water substitution in the binding process. The drug and host interaction phenomenon deciphers the hydrophilicity of carnosine nanoclusters. The X-ray diffraction and optical reflection confirmed the self-assembling process. From, the current *in silico* experimentation and validations, it could be assumed that C-HZ and C-HH conjugates can be better alternatives than administering PYZ and INH alone. The reactivity parameters as deduced from quantum chemical simulations highlighted their enhanced reactivity and stability patterns. The intermolecular interactions of anti-TB drugs with 4NNI and 5VRL were assessed for their stability, and the same has been validated through molecular docking and MDS

analysis. Therefore, the findings find a paramount interest in exploring carnosine nanoclusters as an efficient drug carrier for the nanodelivery of anti-TB drugs in treating TB.

ASSOCIATED CONTENT

Data Availability Statement

The data supporting this study are available upon request.

ⓢ Supporting Information

The Supporting Information is available free of charge at https://pubs.acs.org/doi/10.1021/acsomega.4c07176.

> Drug target modeling and validation; tertiary structure validation of drug targets; and minimized energy profiles and their optimized structures upon ligand optimization using B3LYP/6-311G ++ (d,p) basis theory set (PDF)

AUTHOR INFORMATION

Corresponding Authors

Anand Anbarasu − *Medical and Biological Computing Laboratory, SBST and Department of Biotechnology, SBST, VIT, Vellore, Tamil Nadu 632 014, India;* ⓞ orcid.org/0000-0003-2216-7488; Email: aanand@vit.ac.in

Saravanan Natarajan − *Department of Biochemistry, ICMR-National Institute for Research in Tuberculosis (NIRT), Chennai 600 031, India;* ⓞ orcid.org/0000-0001-7830-2840; Email: natrajan.s@icmr.gov.in

Authors

Usharani Nagarajan − *Department of Biochemistry, ICMR-National Institute for Research in Tuberculosis (NIRT), Chennai 600 031, India*

Aniket Naha − *Department of Bio-Medical Sciences, School of Bio Sciences and Technology (SBST), Vellore Institute of Technology (VIT), Vellore, Tamil Nadu 632 014, India; Medical Biotechnology and Computational Drug Designing Laboratory, Pushpagiri Research Centre, Pushpagiri Medical Society, Tiruvalla, Kerala 689 101, India*

Gayathri Ashok − *Medical and Biological Computing Laboratory, SBST and Department of Biosciences, SBST, VIT, Vellore, Tamil Nadu 632 014, India*

Angayarkanni Balasubramanian − *Department of Bacteriology, ICMR-National Institute for Research in Tuberculosis (NIRT), Chennai 600 031, India*

Sudha Ramaiah − *Medical and Biological Computing Laboratory, SBST and Department of Biosciences, SBST, VIT, Vellore, Tamil Nadu 632 014, India;* ⓞ orcid.org/0000-0002-4800-329X

Swarna V Kanth − *CHORD, CSIR-Central Leather Research Institute, Chennai 600 020, India;* ⓞ orcid.org/0000-0002-3064-3512

Azger Dusthackeer − *Department of Bacteriology, ICMR-National Institute for Research in Tuberculosis (NIRT), Chennai 600 031, India*

Complete contact information is available at:
https://pubs.acs.org/10.1021/acsomega.4c07176

Author Contributions

U.N. and A.N. have contributed equally to this work. N.U.: Idea and conceptualization methodology, data acquisition, data analysis, interpretation, and writing- manuscript—original draft preparation. A.N.: Methodology, data acquisition, data analysis, interpretation, and writing- manuscript (computational). G.A.: Data acquisition and data analysis (computational). A.B.: Methodology (bacteriology-MIC) and data acquisition resources. S.R.: Methodology (computational) resources, supervision, review, and editing. S.V.K.: Supervision, review and editing, and funding acquisition. A.D.: Methodology (bacteriology-MIC) resources, supervision, review, and editing. A.A.: Methodology (computational) resources, supervision, review, and editing. S.N.: Idea and conceptualization, methodology and interpretation resources, supervision, funding acquisition, and writing—review and editing.

Notes

The authors declare no competing financial interest.
The above work does not involve any animal or human subjects and hence exempted form ethical review (NIRT-IEC ID: 2020 044).

ACKNOWLEDGMENTS

REFERENCES

(1) World Health Organization. *COVID-19 Weekly Epidemiological Update.* 2023, *158*.

(2) World Health Organization. *Infection Prevention and Control of Epidemic- and Pandemic-Prone Acute Respiratory Infections in Health Care.* 2014.

(3) Creswell, J.; Sahu, S.; Blok, L.; Bakker, M. I.; Stevens, R.; Ditiu, L. A Multi-Site Evaluation of Innovative Approaches to Increase Tuberculosis Case Notification: Summary Results. *PLoS One* **2014**, *9* (4), No. e94465.

(4) Nasiruddin, M.; Neyaz, M. K.; Das, S. Nanotechnology-Based Approach in Tuberculosis Treatment. *Tuberc. Res. Treat.* **2017**, *2017*, 1−12.

(5) Caruso, G.; Fresta, C. G.; Fidilio, A.; O'Donnell, F.; Musso, N.; Lazzarino, G.; Grasso, M.; Amorini, A. M.; Tascedda, F.; Bucolo, C.; et al. Carnosine decreases pma-induced oxidative stress and inflammation in murine macrophages. *Antioxidants* **2019**, *8*, 281.

(6) Fleisher-Berkovich, S.; Abramovitch-Dahan, C.; Ben-Shabat, S.; Apte, R.; Beit-Yannai, E. Inhibitory effect of carnosine and n-acetyl carnosine on lps-induced microglial oxidative stress and inflammation. *Peptides.* **2009**, *30*, 1306−1312.

(7) Li, T.; Lu, X.-M.; Zhang, M.-R.; Hu, K.; Li, Z. Peptide-Based Nanomaterials: Self-Assembly, Properties and Applications. *Bioact. Mater.* **2022**, *11*, 268−282.

(8) Colomer, I.; Batchelor-McAuley, C.; Odell, B.; Donohoe, T. J.; Compton, R. G. Hydrogen Bonding to Hexafluoroisopropanol Controls the Oxidative Strength of Hypervalent Iodine Reagents. *J. Am. Chem. Soc.* **2016**, *138* (28), 8855−8861.

(9) Yan, S.; Yao, L.; Kang, B.; Lee, J. Y. Solvent Effect on Hydrogen Bonded Tyr⋯Asp⋯Arg Triads: Enzymatic Catalyzed Model System. *Comput. Biol. Chem.* **2016**, *65*, 140−147.

(10) Usharani, N.; Naha, A.; Anbarasu, A.; Ramaiah, S.; Kanth, S. V.; Natarajan, S. Green Synthesis and Characterization of Water Soluble Nanocarnosine: A Prospective Drug Delivery System. *Appl. Mater. Today* **2023**, *32*, No. 101812.

(11) Vasudevan, K.; Basu, S.; Arumugam, A.; Naha, A.; Ramaiah, S.; Anbarasu, A.; Veeraraghavan, B.Identification of Potential Carboxylic Acid-Containing Drug Candidate to Design Novel Competitive NDM Inhibitors: An in-Silico Approach Comprising Combined Virtual Screening and Molecular Dynamics Simulation. *Res. Prepr.* **2021**, .

(12) Naha, A.; Banerjee, S.; Debroy, R.; Basu, S.; Ashok, G.; Priyamvada, P.; Kumar, H.; Preethi, A. R.; Singh, H.; Anbarasu, A.; Ramaiah, S. Network Metrics, Structural Dynamics and Density Functional Theory Calculations Identified a Novel Ursodeoxycholic Acid Derivative against Therapeutic Target Parkin for Parkinson's Disease. *Comput. Struct. Biotechnol. J.* **2022**, *20*, 4271–4287.

(13) Basu, S.; Joshi, S. M.; Ramaiah, S.; Anbarasu, A. Designing Anti-Microbial Peptides Against Major *β*-Lactamase Enzymes in Clinically Important Gram-Negative Bacterial Pathogens: An In-Silico Study. *Probiotics Antimicrob. Proteins* **2022**, *14* (2), 263–276.

(14) Basu, S.; Debroy, R.; Kumar, H.; Singh, H.; Ramaiah, S.; Anbarasu, A. Bioactive Phytocompounds against Specific Target Proteins of Borrelia Recurrentis Responsible for Louse-borne Relapsing Fever: Genomics and Structural Bioinformatics Evidence. *Med. Vet. Entomol.* **2023**, *37* (2), 213–218.

(15) Naha, A.; Vijayakumar, S.; Lal, B.; Shankar, B. A.; Chandran, S.; Ramaiah, S.; Veeraraghavan, B.; Anbarasu, A. Genome Sequencing and Molecular Characterisation of XDR Acinetobacter Baumannii Reveal Complexities in Resistance: Novel Combination of Sulbactam−Durlobactam Holds Promise for Therapeutic Intervention. *J. Cell. Biochem.* **2021**, *122* (12), 1946–1957.

(16) Miryala, S. K.; Basu, S.; Naha, A.; Debroy, R.; Ramaiah, S.; Anbarasu, A.; Natarajan, S. Identification of Bioactive Natural Compounds as Efficient Inhibitors against Mycobacterium Tuberculosis Protein-Targets: A Molecular Docking and Molecular Dynamics Simulation Study. *J. Mol. Liq.* **2021**, *341*, No. 117340.

(17) Naha, A.; Ramaiah, S. Novel Antimicrobial Peptide SAAP Mutant as a Better Adjuvant to Sulbactam-Based Treatments Against Clinical Strains of XDR Acinetobacter Baumannii. *Probiotics Antimicrob. Proteins* **2024**, *16*, 459.

(18) Miryala, S. K.; Basu, S.; Naha, A.; Debroy, R.; Ramaiah, S.; Anbarasu, A.; Natarajan, S. Datasets Comprising the Quality Validations of Simulated Protein-Ligand Complexes and SYBYL Docking Scores of Bioactive Natural Compounds as Inhibitors of Mycobacterium Tuberculosis Protein-Targets. *Data Br.* **2022**, *42*, No. 108146.

(19) Basu, S.; Veeraraghavan, B.; Ramaiah, S.; Anbarasu, A. Novel Cyclohexanone Compound as a Potential Ligand against SARS-CoV-2 Main-Protease. *Microb. Pathog.* **2020**, *149*, No. 104546.

(20) Varghese, R.; Basu, S.; Neeravi, A.; Pragasam, A.; Aravind, V.; Gupta, R.; Miraclin, A.; Ramaiah, S.; Anbarasu, A.; Veeraraghavan, B. Emergence of Meropenem Resistance Among Cefotaxime Non-Susceptible Streptococcus Pneumoniae: Evidence and Challenges. *Front. Microbiol.* **2022**, *12*, 4111.

(21) Basu, S.; Varghese, R.; Debroy, R.; Ramaiah, S.; Veeraraghavan, B.; Anbarasu, A. Non-Steroidal Anti-Inflammatory Drugs Ketorolac and Etodolac Can Augment the Treatment against Pneumococcal Meningitis by Targeting Penicillin-Binding Proteins. *Microb. Pathog.* **2022**, *170* (7), No. 105694.

(22) Arul, A.; Rana, P.; Das, K.; Pan, I.; Mandal, D.; Stewart, A.; Maity, B.; Ghosh, S.; Das, P. Fabrication of Self-Assembled Nanostructures for Intracellular Drug Delivery from Diphenylalanine Analogues with Rigid or Flexible Chemical Linkers. *Nanoscale Adv.* **2021**, *3* (21), 6176–6190.

(23) Alghamdi, W. A.; Al-Shaer, M. H.; Peloquin, C. A. Protein Binding of First-Line Antituberculosis Drugs. *Antimicrob. Agents Chemother.* **2018**, *62* (7), No. e00641-18.

(24) Nagarajan, U.; Gladstone Christopher, J.; Jonnalagadda, R. R.; Chandrasekaran, B.; Balachandran, U. N. Studies on the Chemico-Biological Characteristics of Bilirubin Binding with Collagen. *Mater. Sci. Eng., C* **2013**, *33* (8), 4965–4971.

(25) Branham, M. L.; Singh, P.; Bisetty, K.; Sabela, M.; Govender, T. Preparation, Spectrochemical, and Computational Analysis of L-Carnosine (2-[(3-Aminopropanoyl)Amino]-3-(1H-Imidazol-5-Yl)-Propanoic Acid) and Its Ruthenium (II) Coordination Complexes in Aqueous Solution. *Molecules* **2011**, *16* (12), 10269–10291.

(26) Abdelkader, H.; Longman, M.; Alany, R.; Pierscionek, B. Phytosome-Hyaluronic Acid Systems for Ocular Delivery of L-Carnosine. *Int. J. Nanomedicine* **2016**, 2815.

(27) Ahmad, T.; Veenu; Nazim, A.; Farooq, U.; Khan, H.; Jain, S. K.; Ubaidullah, M.; Ahmed, J. Biosynthesis, Characterization and Photo-Catalytic Degradation of Methylene Blue Using Silver Nanoparticles. *Mater. Today Proc.* **2020**, *29*, 1039–1043.

(28) Lu, X.; Zhang, Y.; Wang, L.; Li, G.; Gao, J.; Wang, Y. Development of L-Carnosine Functionalized Iron Oxide Nano-particles Loaded with Dexamethasone for Simultaneous Therapeutic Potential of Blood Brain Barrier Crossing and Ischemic Stroke Treatment. *Drug Delivery* **2021**, *28* (1), 380–389.

(29) Masri, A.; Brown, D. M.; Smith, D. G. E.; Stone, V.; Johnston, H. J. Comparison of In Vitro Approaches to Assess the Antibacterial Effects of Nanomaterials. *J. Funct. Biomater.* **2022**, *13* (4), 255.

(30) Thiha, A.; Ibrahim, F. A Colorimetric Enzyme-Linked Immunosorbent Assay (ELISA) Detection Platform for a Point-of-Care Dengue Detection System on a Lab-on-Compact-Disc. *Sensors* **2015**, *15* (5), 11431–11441.

(31) Acuña, S. M.; Veloso, M. C.; Toledo, P. G. Self-Assembly of Diphenylalanine-Based Nanostructures in Water and Electrolyte Solutions. *J. Nanomater.* **2018**, *2018*, 1–7.

(32) Mahapatra, R. Das; Dey, J.; Weiss, R. G. L -Carnosine-Derived Fmoc-Tripeptides Forming PH-Sensitive and Proteolytically Stable Supramolecular Hydrogels. *Langmuir* **2017**, *33* (45), 12989–12999.

(33) Huhtamäki, T.; Tian, X.; Korhonen, J. T.; Ras, R. H. A. Surface-Wetting Characterization Using Contact-Angle Measurements. *Nat. Protoc.* **2018**, *13* (7), 1521–1538.

(34) Makane, V. B.; Krishna, V. S.; Krishna, E. V.; Shukla, M.; Mahizhaveni, B.; Misra, S.; Chopra, S.; Sriram, D.; Dusthackeer, V. N. A.; Rode, H. B. Synthesis and Evaluation of *α*-Aminoacyl Amides as Antitubercular Agents Effective on Drug Resistant Tuberculosis. *Eur. J. Med. Chem.* **2019**, *164*, 665–677.

(35) Kim, S.; Thiessen, P. A.; Bolton, E. E.; Chen, J.; Fu, G.; Gindulyte, A.; Han, L.; He, J.; He, S.; Shoemaker, B. A.; Wang, J.; Yu, B.; Zhang, J.; Bryant, S. H. PubChem Substance and Compound Databases. *Nucleic Acids Res.* **2016**, *44* (D1), D1202–D1213.

(36) Hanwell, M. D.; Curtis, D. E.; Lonie, D. C.; Vandermeersch, T.; Zurek, E.; Hutchison, G. R. Avogadro: An Advanced Semantic Chemical Editor, Visualization, and Analysis Platform. *J. Cheminform.* **2012**, *4* (1), 1–17.

(37) Murail, S.; de Vries, S. J.; Rey, J.; Moroy, G.; Tufféry, P. SeamDock: An Interactive and Collaborative Online Docking Resource to Assist Small Compound Molecular Docking. *Front. Mol. Biosci.* **2021**, *8*, No. 716466.

(38) Schwede, T. SWISS-MODEL: An Automated Protein Homology-Modeling Server. *Nucleic Acids Res.* **2003**, *31* (13), 3381–3385.

(39) Heo, L.; Park, H.; Seok, C. GalaxyRefine: Protein Structure Refinement Driven by Side-Chain Repacking. *Nucleic Acids Res.* **2013**, *41* (Web Serverissue), 384–388.

(40) Kaplan, W.; Littlejohn, T. G. Swiss-PDB Viewer (Deep View). *Brief. Bioinform.* **2001**, *2* (2), 195–197.

(41) Wiederstein, M.; Sippl, M. J. ProSA-Web: Interactive Web Service for the Recognition of Errors in Three-Dimensional Structures of Proteins. *Nucleic Acids Res.* **2007**, *35* (2), 407–410.

(42) Hunter, S.; Apweiler, R.; Attwood, T. K.; Bairoch, A.; Bateman, A.; Binns, D.; Bork, P.; Das, U.; Daugherty, L.; Duquenne, L.; Finn, R. D.; Gough, J.; Haft, D.; Hulo, N.; Kahn, D.; Lopez, R.; Madera, M.; Yeats, C. InterPro: The Integrative Protein Signature Database. *Nucleic Acids Res.* **2009**, *37* (Database), D211–D215.

(43) Bateman, A.; Coin, L.; Durbin, R.; Finn, R. D.; Hollich, V.; Griffiths-Jones, S.; Khanna, A.; Marshall, M.; Moxon, S.; Sonnhammer, E. L.; Studholme, D. J. The Pfam Protein Families Database. *Nucleic Acids Res.* **2004**, *32* (1), D138–D141.

(44) Tian, W.; Chen, C.; Lei, X.; Zhao, J.; Liang, J. CASTp 3.0: Computed Atlas of Surface Topography of Proteins. *Nucleic Acids Res.* **2018**, *46* (W1), W363–W367.

(45) Hussein, H. A.; Borrel, A.; Geneix, C.; Petitjean, M.; Regad, L.; Camproux, A.-C. PockDrug-Server: A New Web Server for Predicting Pocket Druggability on Holo and Apo Proteins. *Nucleic Acids Res.* **2015**, *43* (W1), W436–W442.

(46) Morris, G. M.; Huey, R.; Lindstrom, W.; Sanner, M. F.; Belew, R. K.; Goodsell, D. S.; Olson, A. J. AutoDock4 and AutoDockTools4: Automated Docking with Selective Receptor Flexibility. *J. Comput. Chem.* **2009**, *30* (16), 2785−2791.

(47) Studio, D. Discovery Studio Modelling Environment. *Dassault Syst. BIOVIA, Accelrys Softw Inc.* **2015**, *4* (5), 98−104.

(48) Pettersen, E. F.; Goddard, T. D.; Huang, C. C.; Couch, G. S.; Greenblatt, D. M.; Meng, E. C.; Ferrin, T. E. UCSF Chimera–a Visualization System for Exploratory Research and Analysis. *J. Comput. Chem.* **2004**, *25* (13), 1605−1612.

(49) Frisch, M. J.; Trucks, G. W.; Schlegel, H. B.; Scuseria, G. E.; Robb, M. A.; Cheeseman, J. R.; Scalmani, G.; Barone, V.; Mennucci, B.; Petersson, G. A.; Nakatsuji, H. *Gaussian 09, Revision A. 2.*; Gaussian, Inc: Wallingford, CT, 2009.

(50) Dennington, R.; Keith, T.; Millam, J. *GaussView, Version 5*; Semichem Inc.: Shawnee Mission, 2009.

(51) Stephens, P. J.; Devlin, F. J.; Chabalowski, C. F.; Frisch, M. J. Ab Initio Calculation of Vibrational Absorption and Circular Dichroism Spectra Using Density Functional Force Fields. *J. Phys. Chem.* **1994**, *98* (45), 11623−11627.

(52) Zacharias, A. O.; Varghese, A.; Akshaya, K. B.; Savitha, M. S.; George, L. DFT, Spectroscopic Studies, NBO, NLO and Fukui Functional Analysis of 1-(1-(2,4-Difluorophenyl)-2-(1H-1,2,4-Triazol-1-Yl)Ethylidene) Thiosemicarbazide. *J. Mol. Struct.* **2018**, *1158*, 1−13.

(53) Naha, A.; Ramaiah, S. Structural Chemistry and Molecular-Level Interactome Reveals Histidine Kinase EvgS to Subvert Both Antimicrobial Resistance and Virulence in Shigella Flexneri 2a Str. 301. *3 Biotech* **2022**, *12* (10), 258.

(54) Lemkul, J. From Proteins to Perturbed Hamiltonians: A Suite of Tutorials for the GROMACS-2018 Molecular Simulation Package [Article v1.0]. *Living J. Comput. Mol. Sci.* **2019**, *1* (1), 1−53.

(55) Jayaraman, M.; Rajendra, S. K.; Ramadas, K. Structural Insight into Conformational Dynamics of Non-Active Site Mutations in KasA: A Mycobacterium Tuberculosis Target Protein. *Gene* **2019**, *720*, No. 144082.

(56) Qiu, J.; Hauske, S. J.; Zhang, S.; Rodriguez-Niño, A.; Albrecht, T.; Pastene, D. O.; van den Born, J.; van Goor, H.; Ruf, S.; Kohlmann, M.; et al. Identification and characterisation of carnostatine (san9812), a potent and selective carnosinase (CN1) inhibitor with in vivo activity. *Amino Acids.* **2019**, *51*, 7−16.

(57) Jackson, M. C.; Kucera, C. M.; Lenney, J. F. Purification and properties of human serum carnosinase. *Clin. Chim. Acta* **1991**, *196*, 193−205.

(58) Tan, Y. H.; Davis, J. A.; Fujikawa, K.; Ganesh, N. V.; Demchenko, A. V.; Stine, K. J. Surface Area and Pore Size Characteristics of Nanoporous Gold Subjected to Thermal, Mechanical, or Surface Modification Studied Using Gas Adsorption Isotherms, Cyclic Voltammetry, Thermogravimetric Analysis, and Scanning Electron Microscopy. *J. Mater. Chem.* **2012**, *22* (14), 6733−6745.

(59) Beebe, A.; Seaworth, B.; Patil, N. Rifampicin-Induced Nephrotoxicity in a Tuberculosis Patient. *J. Clin. Tuberc. Other Mycobact. Dis.* **2015**, *1*, 13−15.

(60) Zargarnezhad, S.; Gholami, A.; Khoshneviszadeh, M.; Abootalebi, S. N.; Ghasemi, Y. Antimicrobial Activity of Isoniazid in Conjugation with Surface-Modified Magnetic Nanoparticles against Mycobacterium Tuberculosis and Nonmycobacterial Microorganisms. *J. Nanomater.* **2020**, *2020*, 1−9.

(61) Ren, Z-y; Wan, Q-q; Zhu, Y-n; et al. Atypical artificial cells: novel biomimetic materials for combating cancer. *Interdiscip Mater.* **2024**, *3*, 658−714.